Causes of the Arctic's Lower-Tropospheric Warming Structure

ZACHARY S. KAUFMAN[a] AND NICOLE FELDL[a]

[a] *University of California, Santa Cruz, Santa Cruz, California*

(Manuscript received 14 April 2021, in final form 11 December 2021)

ABSTRACT: Arctic amplification has been attributed predominantly to a positive lapse rate feedback in winter, when boundary layer temperature inversions focus warming near the surface. Predicting high-latitude climate change effectively thus requires identifying the local and remote physical processes that set the Arctic's vertical warming structure. In this study, we analyze output from the CESM Large Ensemble's twenty-first-century climate change projection to diagnose the relative influence of two Arctic heating sources, local sea ice loss and remote changes in atmospheric heat transport. Causal effects are quantified with a statistical inference method, allowing us to assess the energetic pathways mediating the Arctic temperature response and the role of internal variability across the ensemble. We find that a step-increase in latent heat flux convergence causes Arctic lower-tropospheric warming in all seasons, while additionally reducing net longwave cooling at the surface. However, these effects only lead to small and short-lived changes in boundary layer inversion strength. By contrast, a step-decrease in sea ice extent in the melt season causes, in fall and winter, surface-amplified warming and weakened boundary layer temperature inversions. Sea ice loss also enhances surface turbulent heat fluxes and cloud-driven condensational heating, which mediate the atmospheric temperature response. While the aggregate effect of many moist transport events and seasons of sea ice loss will be different than the response to hypothetical perturbations, our results nonetheless highlight the mechanisms that alter the Arctic temperature inversion in response to CO_2 forcing. As sea ice declines, the atmosphere's boundary layer temperature structure is weakened, static stability decreases, and a thermodynamic coupling emerges between the Arctic surface and the overlying troposphere.

KEYWORDS: Arctic; Sea ice; Energy transport; Inversions; Coupled models

1. Introduction

Global climate change is characterized by an Arctic-amplified pattern of surface warming. This warming pattern is a robust feature of climate models subjected to increases in CO_2 (Manabe and Stouffer 1980; Holland and Bitz 2003), and observed Arctic temperatures have warmed at twice the global average in recent decades (Serreze et al. 2009; England et al. 2021). However, considerable uncertainty remains regarding the underlying mechanisms of the Arctic amplification phenomenon (Smith et al. 2019). Accurate predictions of future warming trends require understanding of the various feedback mechanisms acting at high latitudes. The surface albedo feedback associated with sea ice loss has long been understood to shape polar climate sensitivity: melting snow and sea ice increase the surface absorption of solar radiation, leading to additional warming (Manabe and Wetherald 1975). However, the changes in sea ice are largest in summer, while Arctic near-surface warming trends are largest in winter (Lu and Cai 2009), when shortwave radiative fluxes are small. This discrepancy highlights an additional positive feedback, the high-latitude lapse rate feedback, which is associated with the Arctic's surface-amplified warming in the cold season (Winton 2006). More generally, the lapse rate feedback describes the effect of vertically nonuniform tropospheric warming on the efficiency of radiative cooling to space.

The surface-amplified warming characteristic of a positive lapse rate feedback arises in the Arctic due to stable stratification of the wintertime boundary layer, which inhibits upward mixing of thermal anomalies away from the surface (Bintanja et al. 2011). Compared to vertically uniform warming, this bottom-heavy structure necessitates larger surface temperature increases to drive the change in outgoing longwave radiation that balances anthropogenic CO_2 forcing (i.e., a positive lapse rate feedback). This situation can be contrasted with the tropics, where deep convection leads CO_2-forced warming to maximize in the upper troposphere, producing more efficient radiative cooling and a negative lapse rate feedback. Therefore, the spatial pattern of lapse rate changes drives Arctic amplification in fully coupled climate models (Pithan and Mauritsen 2014; Stuecker et al. 2018), as well as hemispheric asymmetries in projected polar warming, where the Arctic exhibits greater warming than the Antarctic (Hahn et al. 2020).

Although the physical basis for the positive high-latitude lapse rate feedback is well established, its coupled interactions with other aspects of the climate system remain unclear. From a local perspective, quantifying the warming contribution of the Arctic lapse rate feedback is challenging because of its interdependent relationship with sea ice. Reductions in ice cover during the warm season can lead to a buildup of heat in the newly exposed ocean, delaying freeze-up in fall and winter (Serreze et al. 2007b, 2009; Boeke and Taylor 2018). This stored heat can then be released to the overlying near-surface atmosphere via enhanced upward turbulent heat fluxes (Manabe and Stouffer

Supplemental information related to this paper is available at the Journals Online website: https://doi.org/10.1175/JCLI-D-21-0298.s1.

Corresponding author: Zachary S. Kaufman, zskaufma@ucsc.edu

DOI: 10.1175/JCLI-D-21-0298.1

1980; Bintanja and van der Linden 2013; Dai et al. 2019; Feldl et al. 2020). Supporting this coupled mechanism, modeling experiments that disable or suppress the ice-albedo feedback have shown a corresponding reduction in the polar lapse rate feedback (Graversen et al. 2014; Feldl et al. 2017a).

In addition to local feedbacks, remote processes may also influence Arctic warming through the poleward transport of heat and moisture. Although twenty-first-century climate change simulations project only small increases in net atmospheric heat transport into the Arctic, compensating decreases in dry static energy transport (Hwang et al. 2011) and increases in latent heat transport (Held and Soden 2006) can be much larger. Beyond the effect of latent heating upon condensation, remotely sourced moisture can contribute to Arctic warming through the water vapor and cloud feedbacks, which increase the infrared opacity of the atmosphere and tend to strengthen downward longwave radiative fluxes (Lee et al. 2017; Yoshimori et al. 2017; Graversen and Langen 2019). These impacts of latent heat transport on the surface radiation budget have been implicated in Arctic warming and sea ice trends (D.-S. R. Park et al. 2015; H.-S. Park et al. 2015; Gong et al. 2017). Further, a tropical mechanism causing Arctic warming has been identified in models forced by prescribed tropical sea surface temperatures (SSTs; Ding et al. 2014; Dong et al. 2019). The tropically excited Arctic warming mechanism has been used to explain observed wintertime near-surface Arctic warming, where anomalous deep convection over the west Pacific promotes Rossby wave propagation toward higher latitudes during the La Niña phase of El Niño–Southern Oscillation (Lee 2012; Liu and Barnes 2015; Baggett and Lee 2017). Finally, remotely sourced Arctic warming can be accomplished by anomalous ocean heat transport, which has been shown to drive multiyear sea ice declines in many climate models, particularly along continental shelves (Auclair and Tremblay 2018). However, meridional energy flux convergence into the Arctic is dominated by the atmospheric component (Serreze et al. 2007a), which is the primary focus of our study.

The complex interplay between local feedbacks and remote heat transport hampers efforts to isolate the contribution of an individual process to Arctic warming. Overcoming this difficulty requires identifying the changes in the Arctic troposphere that are ultimately local or remote in origin. As demonstrated by Feldl et al. (2020), a partitioning of the lapse rate feedback into upper and lower contributions reveals that lower-tropospheric warming is strongly tied to climatological sea ice extent and sea ice loss, enhancing the positive lapse rate feedback, while remotely driven increases in heat transport warm the midtroposphere, weakening the lapse rate feedback in subpolar latitudes. Similar interactions between the lapse rate feedback and atmospheric heat transport have been previously noted by Feldl et al. (2017b) and Stuecker et al. (2018). Crucially, this remote influence on the high-latitude lapse rate feedback does not preclude a warming influence on the Arctic surface due to the aforementioned moist transport effects. Direct attributions of polar atmospheric temperature change in a single-column model emphasize the role of CO_2 and water vapor in warming the surface and atmospheric heat transport in warming the mid- and upper troposphere, with compensating behavior by the dry heat transport in the presence of a surface heat source (Henry et al. 2021). Last, it is well established that enhanced atmospheric heat transport is able to produce Arctic amplification in simulations that have meridionally uniform radiative feedbacks (Merlis and Henry 2018; Armour et al. 2019), suppress the ice-albedo feedback (Graversen and Wang 2009), or lack sea ice altogether (Alexeev et al. 2005), although there is some evidence that this response may be due in part to the idealized nature of the simulations (Kim et al. 2018). Attributions of polar amplification are thus represented differently across models of varying complexity and for different attribution methods.

A pressing challenge in climate science is to understand how sea ice and atmospheric circulation interactively set the Arctic's vertical warming structure during the twenty-first century. Using a statistical causal inference approach, we evaluate coupled relationships and causal pathways between time series of sea ice concentration, Arctic atmospheric temperatures, surface energy fluxes, and meridional heat flux convergence from output of the Community Earth System Model. Although CO_2 forcing is the ultimate driver of Arctic warming, we seek to identify and quantify the proximate causes and mediating pathways between sea ice and heat-transport perturbations and the eventual warming response in a comprehensive model. Such pathways are uncovered using causal network learning algorithms that analyze large numbers of interdependent time series variables at once (Pearl 2000; Spirtes et al. 2000). These novel statistical techniques are just beginning to be applied to the study of Arctic climate (Kretschmer et al. 2016) and their adaptation for geoscience applications is a new and active area of research (Runge et al. 2019). By evaluating the Arctic's temperature inversion in a fully coupled setting, we account for two-way relationships among the physical processes of interest. This is a crucial feature of our analysis, as sea ice and atmospheric circulation do not control Arctic climate independently; sea ice loss, for instance, can itself drive circulation changes in both the atmosphere (Screen et al. 2018; McGraw et al. 2020) and the ocean (Tomas et al. 2016). Our statistical approach therefore disentangles the atmosphere–ocean–ice interactions underlying the high-latitude lapse rate feedback and Arctic amplification.

2. Methods

a. Climate model output and diagnostics

This study is conducted with output from the Community Earth System Model Large Ensemble (CESM-LE; Kay et al. 2015). The CESM-LE climate change simulation is initialized from an equilibrium preindustrial control state, then subjected to historical greenhouse gas forcing from 1920 to 2005 and projected forcing from 2005 to 2100 using the RCP8.5 climate forcing scenario. For our analyzed climate fields, we utilize output spanning 1986–2100. Over this time period, the CESM-LE simulates 40 ensemble members with the same underlying physics, but each member's air temperature fields

TABLE 1. List of the causal network input variables described in section 2a, along with the spatial averaging region used for each time series. Where relevant, parenthesized variable names denote abbreviations used in subsequent figures. Note that turbulent heat flux is defined as the sum of sensible and latent heat flux at the surface.

Variable	Vertical domain	Horizontal domain
Sensible heat flux convergence ($-\nabla_{850} \cdot c_p[\overline{vT}]$)	850 hPa	70°–90°N
Latent heat flux convergence ($-\nabla_{500} \cdot L[\overline{vq}]$)	500 hPa	70°–90°N
Boundary layer atmospheric temperature (T_{850})	850 hPa	1986–96 annual mean sea ice edge (15% concentration contour)
Boundary layer inversion strength	$T_{850} - T_{2m}$	1986–96 annual mean sea ice edge (15% concentration contour)
Net all-sky longwave radiative flux (LW_{net})	Surface	1986–96 annual mean sea ice edge (15% concentration contour)
Net all-sky shortwave radiative flux (SW_{net})	Surface	1986–96 annual mean sea ice edge (15% concentration contour)
Shortwave cloud radiative effect (SW_{CRE})	Surface	1986–96 annual mean sea ice edge (15% concentration contour)
Longwave cloud radiative effect (LW_{net})	Surface	1986–96 annual mean sea ice edge (15% concentration contour)
Turbulent heat flux	Surface	1986–96 annual mean sea ice edge (15% concentration contour)
Sea ice extent	Surface	1986–96 annual mean sea ice edge (15% concentration contour)

are given slightly differing initial conditions, providing a tool to assess the role of internal variability in climate change projections. By applying our analysis across ensemble members, we can analyze both the forced climate response, represented by the ensemble mean, and internal variability, represented by the ensemble spread.

Our data-driven, causal inference approach applies time series analysis to the CESM-LE model output, where the variables of interest are simultaneously represented in a large, inclusive network for each ensemble member. Causal network input consists of 10 spatially averaged time series, which track various aspects of the high-latitude climate system. Each variable and its spatial averaging domain are listed in Table 1. Four atmospheric variables are used, two of which represent Arctic temperatures at different altitudes in the troposphere, and two that represent components of meridional energy transport into the high latitudes. Surface energy fluxes and sea ice extent are represented by the remaining six time series variables. In this section, we provide a physical description of each term within the context of the RCP8.5 scenario.

In all ensemble members, the annual-mean Arctic warming response to RCP8.5 forcing is largest below 850 hPa, dictated primarily by changes in the wintertime vertical temperature structure (Fig. 1a). At the end of the twentieth century, the Arctic is characterized by stable stratification in the boundary layer; temperature increases with height throughout the lower portion of the atmosphere in all seasons, with strong inversions occurring in winter (DJF) and spring (MAM). By the end of the twenty-first century, surface-amplified warming fully erodes the boundary layer temperature inversions in fall (SON) and winter (DJF), with winter experiencing the largest change in inversion strength. Hence, to characterize the vertically nonuniform Arctic temperature changes, our causal networks include 850-hPa temperature (T_{850}) and inversion strength variables, where inversion strength is estimated as the difference between T_{850} and near-surface (2 m) temperature.

Changes in remotely sourced heat and moisture into the high latitudes are evaluated using the horizontal convergence of latent and sensible heat fluxes, $-\nabla \cdot L\mathbf{v}q$ and $-\nabla \cdot c_p\mathbf{v}T$, respectively. At a given pressure (p) level, the meridional convergence of zonal mean heat flux is then given by

$$-\nabla_p \cdot L[\overline{vq}] = \frac{-1}{R\cos\phi}\frac{\partial}{\partial\phi}(L[\overline{vq}]\cos\phi), \tag{1}$$

$$-\nabla_p \cdot c_p[\overline{vT}] = \frac{-1}{R\cos\phi}\frac{\partial}{\partial\phi}\left(c_p[\overline{vT}]\cos\phi\right), \tag{2}$$

where L is the latent heat of vaporization (2.51×10^6 J kg^{-1}), c_p is the specific heat capacity of air at constant pressure (1004 J kg^{-1} K^{-1}), v is meridional wind, q is specific humidity, R is Earth's radius, ϕ is latitude, square brackets denote a zonal mean, and overbars denote a time average. Diagnostic variables $\overline{vq}$ and $\overline{vT}$ are calculated online during simulation at each model time step (30 min) to take cyclonic effects into account, then saved as monthly means. However, analogous transport terms involving geopotential height and zonal wind are not provided for CESM1-LE. Due to this data limitation, we neglect the geopotential energy contribution to dry static energy flux convergence [Eq. (2)], which contributes approximately 29% of the annual mean convergence in the Arctic troposphere (Cardinale et al. 2021). Since we use zonal means in Eqs. (1) and (2), the averaging domain for our two transport terms must be defined in terms of latitude (Table 1). Finally, we neglect the latent heat of freezing for the case of solid precipitation [Eq. (1)], following prior assessments of Arctic latent heat flux convergence in CESM1 (Graversen and Langen 2019).

Climatological, mass-weighted vertical profiles of the two heat flux convergence components, as well as their distinct responses to RCP8.5 forcing, are shown in Figs. 1b and 1c. In the Arctic midtroposphere (800–400 hPa), increases in latent heat flux convergence [Eq. (1)] occur in every season over the twenty-first century, with ensemble-mean changes on the order of 1 W m^{-2} (Fig. 1b). Sensible heat flux convergence [Eq. (2)] trends are largest between 950 and 600 hPa, with ensemble-mean decreases on the order of 10 W m^{-2} that are largest in winter and spring (Fig. 1c). The forced changes in latent heat flux convergence are more robust, despite their smaller magnitude, because the forced changes in sensible

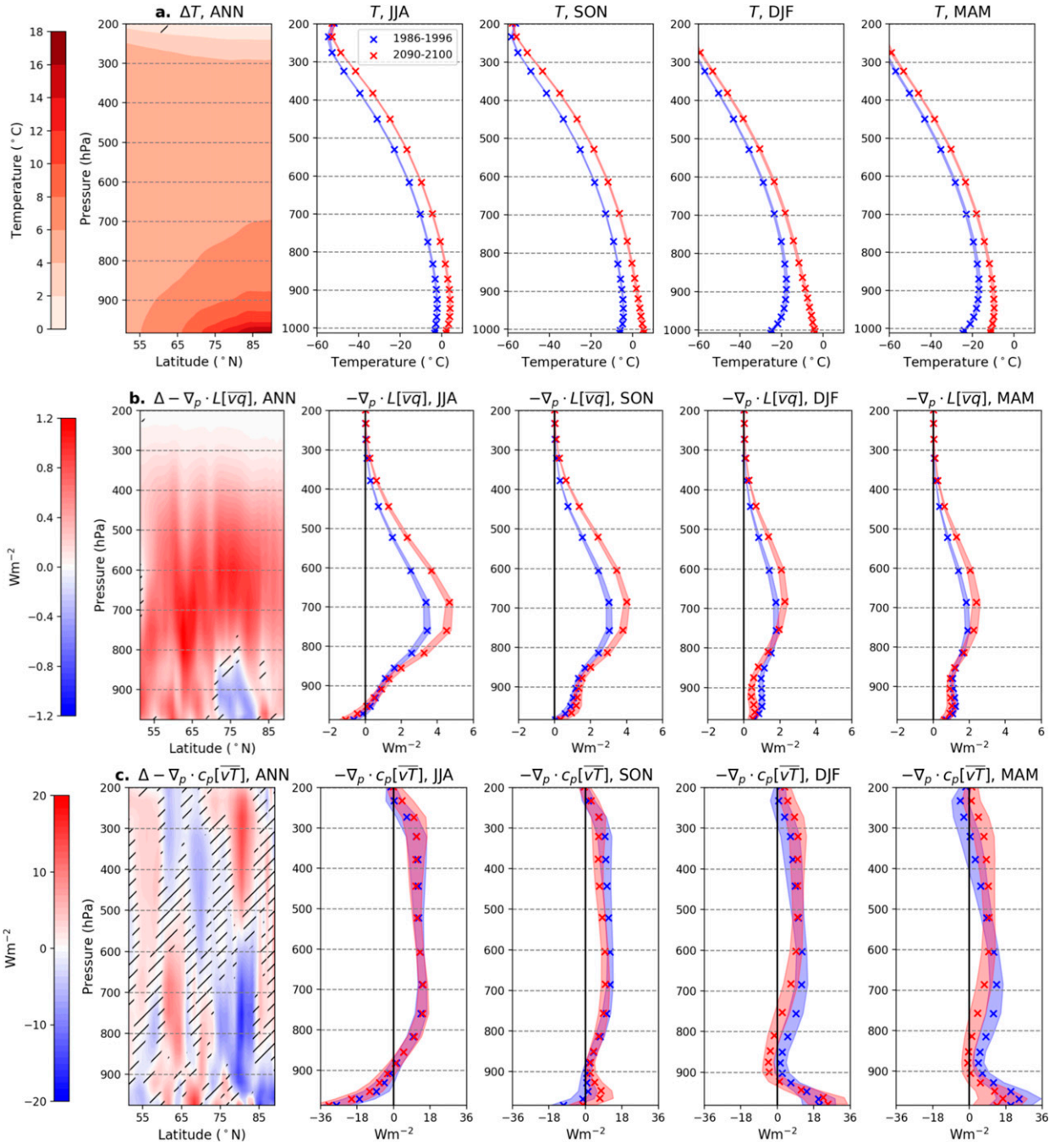

FIG. 1. The twenty-first-century, RCP8.5-forced change in (a) atmospheric temperature (T), (b) zonal-mean latent heat flux convergence ($-\nabla_p \cdot L[\overline{vq}]$), and (c) zonal-mean sensible heat flux convergence ($-\nabla_p \cdot c_p[\overline{vT}]$) in the Community Earth System Model, Large Ensemble (CESM-LE).The leftmost column shows the extratropical zonal-mean, annual-mean difference between the 2090–2100 and 1986–96 climatologies, where color represents the ensemble-mean change, and hatching represents regions where the forced change is insignificant compared to internal variability (two-sided Student's t test, $p = 0.05$). The remaining columns show the Arctic-average (as defined in Table 1) climatologies in 1986–96 (blue) and 2090–2100 (red) for each season, where the x marks indicate the ensemble mean and shaded envelopes indicate the ensemble spread ($\pm 2\sigma$). In (b) and (c), heat flux convergences are mass-weighted by the pressure thickness (dp/g) at each model level (hybrid sigma coordinates).

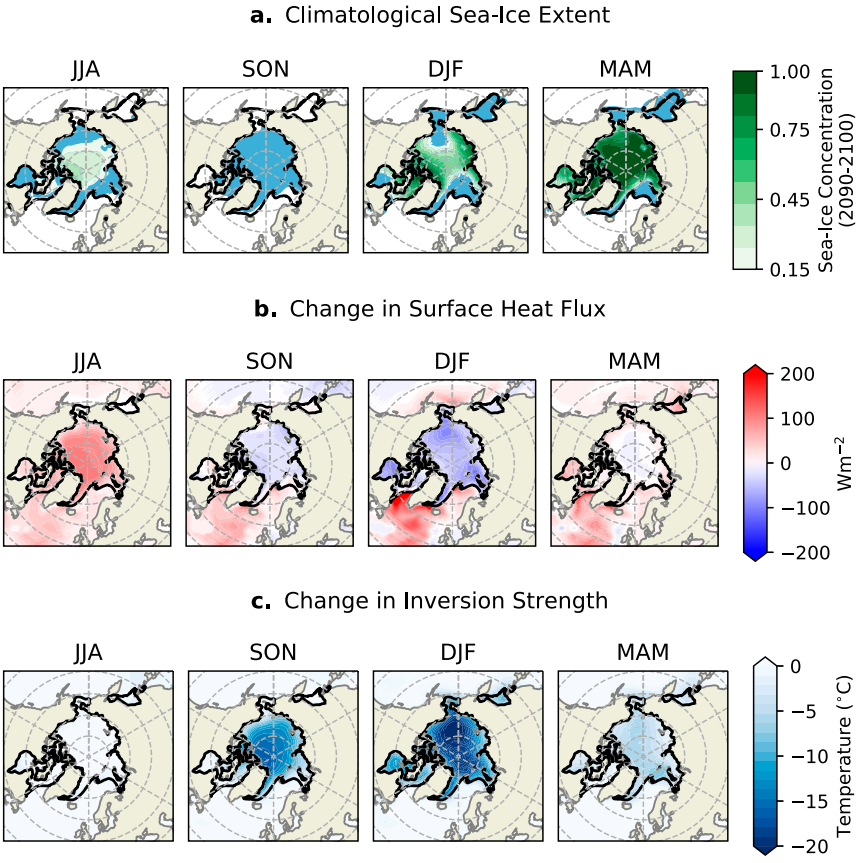

FIG. 2. The twenty-first-century, RCP8.5-forced change in (a) sea ice extent, (b) net surface heat flux ($SW_{net} - LW_{net}$ − turbulent heat flux; positive down), and (c) boundary layer inversion strength ($T_{850} - T_{2m}$) over ocean regions in the Community Earth System Model, Large Ensemble (CESM-LE). In all maps, the black line represents the annual-mean, ensemble-mean sea ice edge at the start of the study period (1986–96), which corresponds to the spatial averaging domain defined in rows 3–10 of Table 1. In (a), the 2090–2100 ensemble-mean climatological sea ice concentration is shown with green contours for each season. Blue regions indicate where seasonal sea ice concentrations are greater than 15% in the 1986–96 climatology. In (b) and (c), ensemble mean changes in surface heat flux and inversion strength, respectively, are shown as the difference between the 2090–2100 and 1986–96 climatologies. Latitude circles (dashed) are shown in 10° intervals for 50°–90°N.

heat flux convergence lie largely within the internal variability. Taken together, midtroposphere changes reflect a large-scale response to anthropogenic forcing, where latent heat flux convergence follows a strengthened meridional humidity gradient (not shown) and sensible heat flux convergence follows a weakened meridional temperature gradient (Fig. 1a). At lower altitudes, below 800 hPa, decreases in net heat flux convergence suggest an additional influence from local surface conditions. For instance, the atmospheric response to sea ice loss has been connected to enhanced local moisture export from the Arctic (Singh et al. 2017) and equatorward mixing of thermal anomalies over adjacent continents (Deser et al. 2010), consistent with the change from sensible heat flux convergence to divergence in winter under RCP8.5 forcing (Fig. 1c). We aim for our causal networks to evaluate changes in heat and moisture at heights where RCP8.5 trends are largest. The networks therefore employ time series of latent heat flux convergence at 500 hPa and sensible heat flux convergence at 850 hPa. For both components, Arctic heat flux convergence is defined as the average over 70°–90°N, following prior research on atmospheric energy transport in CESM1 (Graversen and Langen 2019).

Sea ice extent is defined in terms of its total Northern Hemisphere surface area, which is calculated as an area-weighted sum of grid cell sea ice concentration. The change in sea ice extent over the twenty-first century is shown in Fig. 2a for the ensemble mean. By 2100, fall (SON) sea ice coverage is completely lost in the Northern Hemisphere (<0.1 million km^2) for all ensemble members, while the central Arctic remains ice-covered in the remaining seasons. Spring (MAM) retains the largest sea ice area in 2100 (12.3–14.2 million km^2), largely due to slower melt rates relative to summer (JJA) and

winter (DJF). To coherently assess the atmospheric response to sea ice loss, all surface and lower-tropospheric variables are averaged over ocean areas with at least 15% sea ice in the 1986–96 annual mean (black line, Fig. 2). This limitation excludes high-latitude regions that are perennially ice free at the start of the twenty-first century, but includes areas that become seasonally ice free under RCP8.5 forcing (blue regions, Fig. 2a). All regimes within this spatial domain feature an increase in surface heat uptake in summer (JJA; Fig. 2b) and release to the atmosphere in fall and winter (SON and DJF; Fig. 2b). Decreases in inversion strength closely follow the increases in upward surface heat flux (SON and DJF; Fig. 2c), which occur poleward of the climatological ice edge. Significant inversion strength changes thus take place over both regions that are ice-covered (i.e., the central Arctic) and ice-free (i.e., Hudson Bay) by 2100. This spatial pattern of surface and lower-tropospheric changes is robust across ensemble members and across smaller thresholds for defining the ice line (5% and 10%; not shown).

For the causal network inputs listed in Table 1, the surface energy budget is described using five variables. The sum of surface sensible and latent turbulent heat fluxes provides the first surface variable, upward turbulent heat flux. The second and third surface time series represent the shortwave radiation budget: net shortwave radiative flux at the surface and shortwave (SW_{net}) cloud radiative effect (SW_{CRE}), with the latter quantity calculated as the difference between all-sky and clear-sky net surface shortwave flux. Net longwave surface flux (LW_{net}) and cloud radiative effect (LW_{CRE}) are calculated similarly to the shortwave variables, where a positive LW_{CRE} is a surface warming tendency, consistent with the climatological effect of Arctic clouds. Throughout this study, all surface energy budget terms are defined as positive down (into the surface).

b. Causal networks

Causal networks are constructed from the 10 aforementioned time series, using a linear application of Pearl's causal effect theory (Pearl 2013; Runge et al. 2015). To compare the impact of local and remote warming sources simultaneously, we must select a temporal resolution that accommodates both the short (daily) time scale of variability for midtroposphere heat flux convergence, as well as the longer (monthly) time scale of variability for Arctic sea ice extent. We find that averaging daily CESM-LE output into weekly [i.e., quarter-monthly, as in Kretschmer et al. (2016)] time steps best accomplishes this goal. Assessing causal relationships also requires stationary time series input, so we next remove the anthropogenic trend from each variable. The trend is estimated as a second-order polynomial and subtracted from the data, applied separately for each week in the seasonal cycle. Then, each variable is divided by its standard deviation. The resulting time series input consists of weekly standardized anomalies with constant mean and variance, shown in Fig. 3 for a characteristic ensemble member. Temporal periodicity remains present when there are large seasonal differences in the magnitude of anomalies, which is especially apparent in the shortwave surface fluxes (Figs. 3f,g). This seasonality is a key consideration throughout our analysis. In general, anomalies are an order of magnitude smaller than CO_2-forced trends over 1986–2100. Sensible heat flux convergence (Fig. 3a) is the one exception to this relationship, as its twenty-first-century trends are smaller than its anomalies. The process of constructing causal networks from these time series occurs in two phases. First, we identify the robust, time-lagged causal relationships between each variable in a CESM ensemble member. Then, we quantify causal effects using a linear vector autoregressive (VAR) model.

Causal links between each variable are identified using the PC-algorithm adapted for time series, named after its creators Peter Spirtes and Clark Glymour (PC-Stable; Spirtes et al. 2000). For each input variable, the algorithm begins by calculating every possible time-lagged linear autocorrelation and cross-correlation over a predetermined time window, or maximum lag (τ_{max}). The linear lagged correlation measure is defined as

$$\rho\big[X_i(t-\tau), X_j(t)\big], \tag{3}$$

where ρ is the Pearson correlation coefficient, τ is a time lag (weeks), $X_j(t)$ is one of the 10 input time series variables defined in section 2a, and $X_i(t-\tau)$ are lagged time series with a potential causal influence on $X_j(t)$. Contemporaneous links are not considered in this study. The significance of ρ is assessed with a predefined significance threshold α; if ρ is found to be insignificant, then we conclude that $X_i(t-\tau)$ does not cause $X_j(t)$ and remove it from the set of possible links. We test several values for α and find that $\alpha = 0.01$ provides the optimal balance between network simplicity and network connectivity. Our choices for τ_{max} are discussed in section 3a.

While $X_i(t-\tau)$ may be unconditionally correlated with $X_j(t)$, the relationship could be confounded by the influence of another network variable. Therefore, after the initial lagged correlation test, the PC-algorithm tests the remaining significant links a second time, conditioned on the influence of a third process, Z_1:

$$\rho\big[X_i(t-\tau), X_j(t) | Z_1\big], \tag{4}$$

where $Z_1 \neq X_i(t-\tau)$ is the auto- or cross-link possessing the strongest unconditional correlation with $X_j(t)$ in Eq. (3). The vertical line in Eq. (3) denotes removing the linear influence of Z_1 from both $X_i(t-\tau)$ and $X_j(t)$ and testing the correlation between their residuals. If Z_1 makes the formerly significant link insignificant, the two variables are said to be conditionally independent, and the link is subsequently removed. This process is repeated over n iterations by adding an increasingly stringent number of conditions, $Z_2, Z_3, \ldots, Z_n$ to the partial correlation tests until no more links can be removed. The PC-algorithm finishes when it converges to a final set of significant links for each variable, which are subsequently considered the causes of $X_j(t)$. This designation is based on the causal Markov condition, which states that X_j is independent of all network variables, except X_j's effects, when conditioned on the causes of X_j (Spirtes et al. 2000). The PC-algorithm thus accounts for all indirect and confounding causal connections

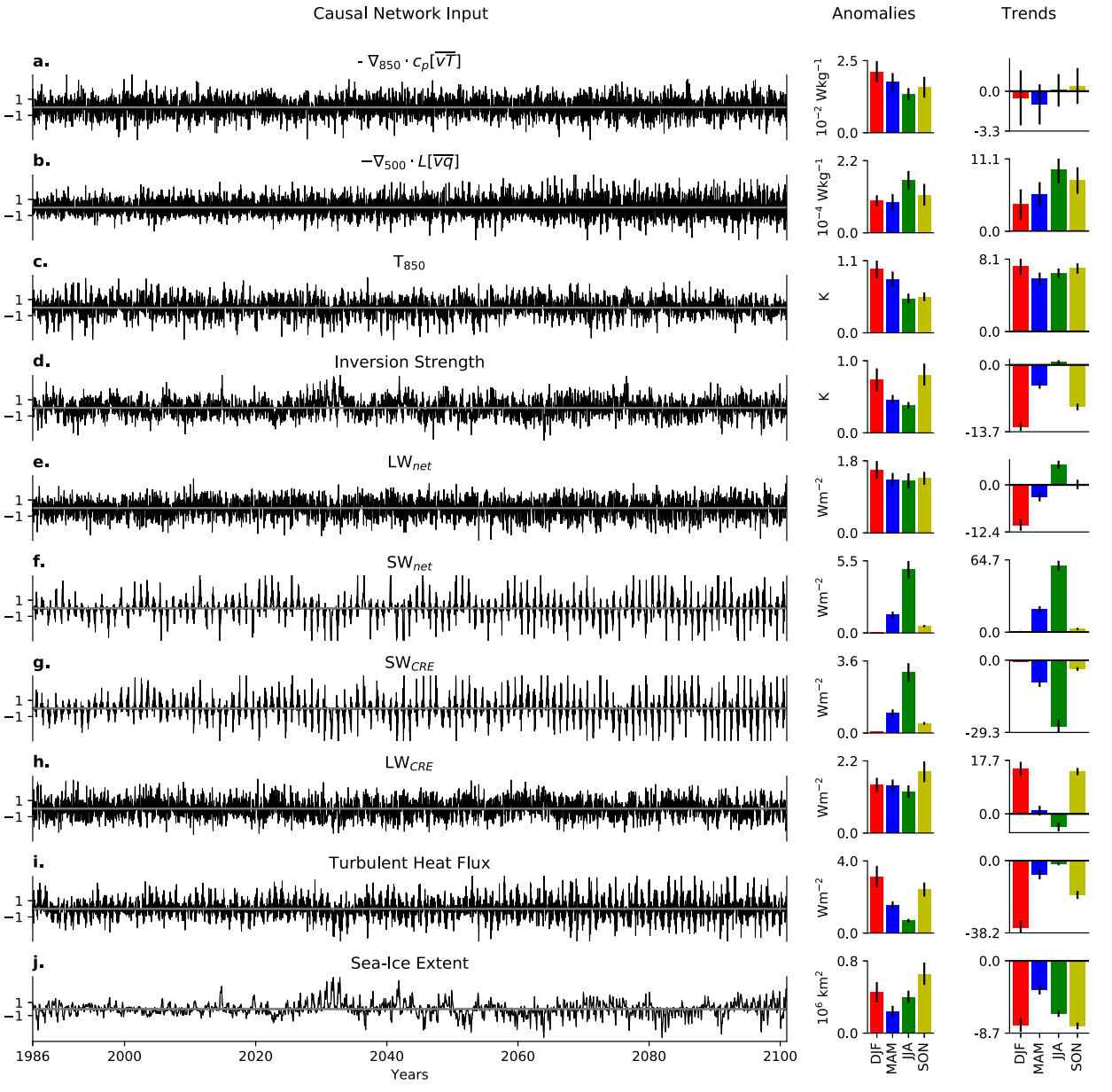

FIG. 3. Weekly time series of causal network inputs, standardized and detrended, shown for a characteristic ensemble member in the Community Earth System Model, Large Ensemble (CESM-LE). (a)–(j) The spatially averaged variables defined in Table 1. For each variable, bar plots display the magnitude of ensemble-mean 1σ anomalies and RCP8.5 trends (1986–2100) for each season. Bar plot error bars represent the ensemble spread, calculated as in Fig. 1. Trends in all surface energy budget terms [(e)–(i)] are signed positive down (into the surface). Note that mass weighting is not applied to submonthly heat flux convergences [(a) and (b)], so trends and anomalies are shown in W kg^{-1}. Products $\overline{vq}$ and $\overline{vT}$ are calculated as weekly averages from daily diagnostic output for v, q, and T at 850 and 500 hPa.

in the complex network, assuming all relevant variables for the system are included. This assumption, which is usually violated to some degree in practice, emphasizes the importance of the variable selection process, as well as the need for prior physical knowledge about the system in question.

Finally, after uncovering each variable's causal predictors with the PC-algorithm, we quantify causal effects following Runge et al. (2015), using a VAR model:

$$\mathbf{X}(t) = \sum_{\tau=1}^{\tau_{\max}} \mathbf{\Phi}(\tau)\mathbf{X}(t-\tau) + \boldsymbol{\epsilon}_t, \tag{5}$$

where $\mathbf{X}$ is a vector of shape (N, t) containing time series for N variables, $\mathbf{\Phi}$ is a standardized regression coefficient matrix of shape $(N, N, \tau_{\max})$, and $\boldsymbol{\epsilon}_t$ are independent, identically distributed error terms, which describe the uncorrelated probability distributions of each causal network variable's anomalies

(Fig. 3). An individual regression coefficient, or link coefficient, $\Phi_{j,i}(\tau)$, indicates the expected change in variable $X_j(t)$ caused by a hypothetical 1σ perturbation in $X_i(t - \tau)$ with all other variables held constant. The term $\tau_{\max}$ refers to the time domain over which link coefficients are added. The VAR model defined in Eq. (5) bears some resemblance to Green's functions used in prior polar climate studies (Kostov et al. 2017), which quantify a climate variable's response to a hypothetical step-increase in a given forcing. However, Eq. (5) additionally utilizes causal inference to account for coupled interactions modulating the response. For instance, $\Phi_{j,i}(\tau) = 0$ unless $X_i(t - \tau)$ causes $X_j(t)$, as determined by the PC-algorithm. This key feature of matrix $\mathbf{\Phi}$ frees the VAR model from having to fit negligible parameters, thus allowing it to accommodate a large number of variables. The link coefficient structure in $\mathbf{\Phi}$ also serves as the causal network, tracing pathways between an imposed perturbation to any variable and the expected temperature response. We construct these networks for each CESM ensemble member using Eqs. (3)–(5), and then analyze their structure to understand the causes of the Arctic's changing temperature inversion.

A visual schematic of a causal network, as well as its associated causal effects, is shown in Fig. 4. The total causal effect [$\mathbf{TCE}(\tau)$] of any hypothetical perturbation is calculated by iteratively computing link coefficient matrix products from a causal network [$\mathbf{\Phi}$; Eq. (5)], given by

$$\mathbf{TCE}(\tau) = \sum_{s=1}^{\tau} \mathbf{\Phi}(s)\mathbf{TCE}(\tau - s). \tag{6}$$

The term $\mathrm{TCE}_{j,i}(\tau)$ represents the total causal effect of perturbed variable $[X_i(t - \tau)]$ on a response variable $[X_j(t)]$. It should be noted that the structures of Eqs. (5) and (6) are similar. Equation (5) is a full description of the causal network, where regression coefficients are calculated from 1 to $\tau_{\max}$. Equation (6) highlights that causal effects can be calculated for any lag in the network, where each effect is the sum of regression coefficients up to (and only to) that specified time lag. We also use this framework to isolate the portion of a causal effect mediated by an intermediate network variable, defined as X_k. This calculation is accomplished by first setting all link coefficients through X_k to zero in matrix $\mathbf{\Phi}$ [Eq. (5)], resulting in a modified coefficient matrix $\mathbf{\Phi}^k$. We then repeat the total causal effect calculation [Eq. (6)] with this modified matrix. The difference between the modified and unmodified calculations yields the mediated causal effect, defined as

$$\mathrm{MCE}^k_{j,i}(\tau) = \mathrm{TCE}_{j,i}(\tau) - \mathrm{TCE}^k_{j,i}(\tau), \tag{7}$$

where $\mathrm{MCE}^k_{j,i}(\tau)$ represents the causal effect of $X_i(t - \tau)$ on $X_j(t)$ mediated by network variable X_k. Note that $\mathrm{MCE}^k_{j,i}(\tau)$ is equal to $\mathrm{TCE}_{j,i}(\tau)$ if $X_k = X_j$. Relatedly, if $X_k = X_i$, then $\mathrm{MCE}^k_{j,i}(\tau)$ indicates the contribution of autocorrelation (memory) in the perturbation of X_i.

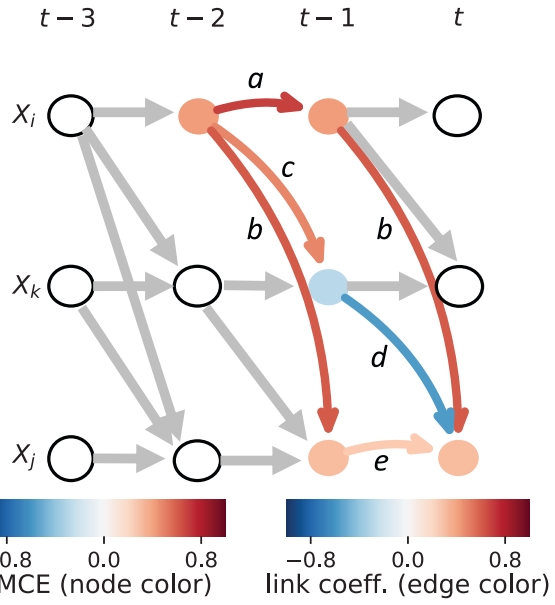

$$TCE_{j,i}(2) = ab + cd + be$$

$$MCE^k_{j,i}(2) = cd$$

FIG. 4. Schematic of a causal network time series graph, as introduced in Runge et al. (2015). Causal pathways are defined by the set of all arrows (gray and colored) and are quantified as the regression coefficient matrix of a VAR model [$\mathbf{\Phi}$, Eq. (5)] with $N = 3$ variables (X_i, X_k, X_j) and $\tau_{\max} = 3$ weeks. Curved, colored arrows denote the specific pathways used to quantify the total causal effect of $X_i(t - 2)$ on $X_j(t)$ [$\mathrm{TCE}_{j,i}(2)$, Eq. (6)] and the causal effect mediated by intermediate variable X_k [$\mathrm{MCE}^k_{j,i}(2)$, Eq. (7)]. In this example, the link coefficient pathway quantifying MCE [cd, blue node at $X_k(t - 1)$] reduces the magnitude of TCE ($ab + cd + be$) because the effects are opposite in sign. Many potential causal links are not shown, as they are deemed insignificant by the PC algorithm [Eqs. (3) and (4)] and excluded from the causal network, such as X_j causing X_k at any lag. Note that the color of affected nodes is constant for each variable (row), as it corresponds to MCE solely for the lag where the perturbation is initiated ($t - 2$, in this case).

3. Results

a. The causal effect of enhanced Arctic heat flux convergence and sea ice loss

In our causal networks, we track remote Arctic warming sources by imposing a hypothetical $+1\sigma$ step increase in 500-hPa Arctic latent heat flux convergence ($-\nabla_{500} \cdot L[\overline{vq}]$) and a -1σ step decrease in 850-hPa sensible heat flux convergence ($-\nabla_{850} \cdot c_p[\overline{vT}]$), with the sign of the perturbations reflecting twenty-first-century anthropogenic trends (Figs. 1b,c). Similarly, a -1σ step decrease in sea ice extent is used to track the local impact of sea ice loss. The

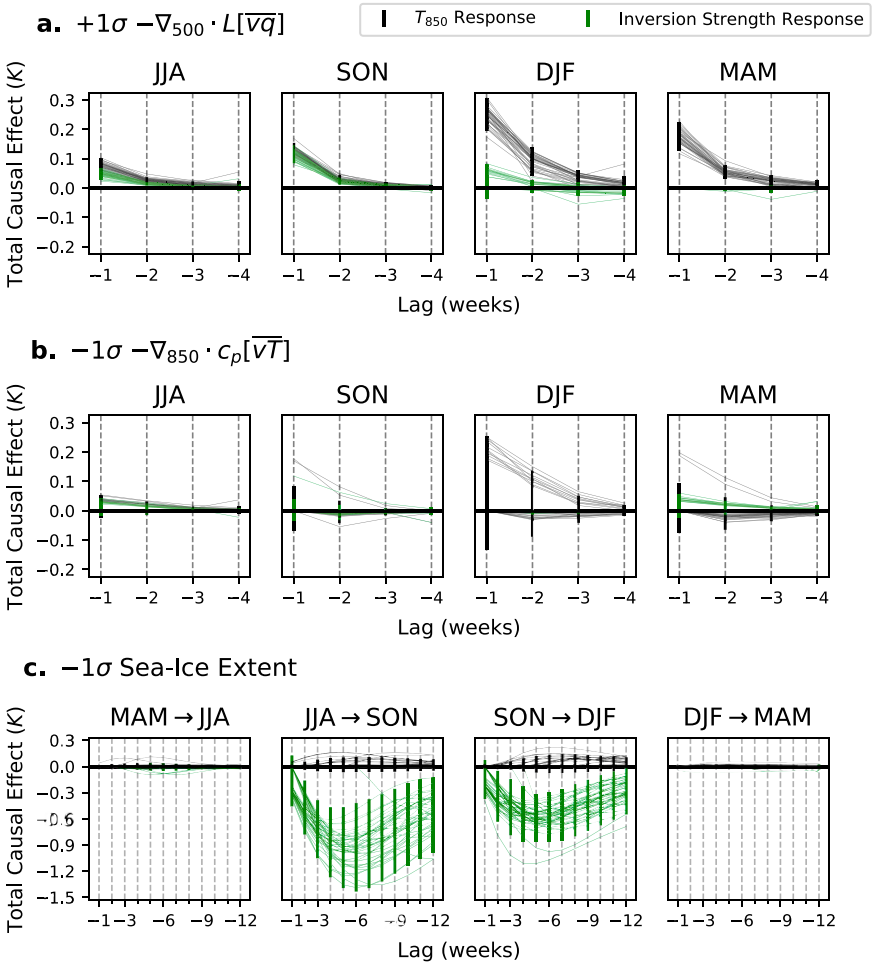

FIG. 5. The predicted change in Arctic atmospheric temperature caused by (a) an imposed $+1\sigma$ step increase in 500-hPa Arctic latent heat flux convergence ($-\nabla_{500} \cdot L[\overline{vq}]$), (b) a -1σ step decrease in 850-hPa sensible heat flux convergence ($-\nabla_{850} \cdot c_p[\overline{vT}]$), and (c) a -1σ step decrease in sea ice extent. In (a) and (b), the 850-hPa temperature response (T_{850}; black) and boundary layer inversion strength response (green) are shown for perturbations at 1–4-week lags in summer (JJA), fall (SON), winter (DJF), and spring (MAM). In (c), the temperature responses are shown for perturbations at 1–12-week lags, across each seasonal transition (note the different y-axis scaling). Curves display the causal effects for individual ensemble members if they are nonzero. At each time lag, vertical error bars denote the spread in estimated causal effect ($\pm 2\sigma$) across 40 CESM ensemble members, where insignificant causal effects are defined as zero.

magnitude of perturbations is equivalent to the annual standard deviation of each detrended time series variable. The total causal effect of each perturbation on 850-hPa Arctic temperature and inversion strength is shown in Fig. 5. To account for the seasonality of Arctic warming, we calculate these causal effects after four separate implementations of the PC-algorithm, where the response variables (850-hPa temperature or inversion strength) are masked to only include data from summer (JJA), fall (SON), winter (DJF), and spring (MAM), respectively, following the approach of Kretschmer et al. (2016). Network regression coefficients are fit for each season using Eqs. (3)–(5). Then, causal effects are calculated at each time lag using Eq. (6). The causal effects analyzed in this section represent the time-lagged linear response of Arctic temperatures to an instantaneous step change in sea ice and/or poleward heat transport. Given the use of detrended time series data, these hypothetical step changes do not describe the transient temperature response to CO_2-forced changes. However, they nonetheless offer the advantage of isolating the impact of individual processes on the lower troposphere in a fully coupled setting.

In Fig. 5a, the total causal effect of enhanced latent heat flux convergence ($+1\sigma - \nabla_{500} \cdot L[\overline{vq}]$) is shown at lags of 1–4 weeks ($\tau = 1$ to $\tau_{max} = 4$) for each CESM ensemble member, where our choice of τ_{max} follows the observed time scale of moist intrusions into the Arctic (Woods et al. 2013). One week following a $+1\sigma$ step increase in latent heat flux

convergence, the Arctic atmosphere responds by warming at 850 hPa in all seasons (black curves), with the total causal effect [$TCE_{j,i}(1)$] ranging from 0.077 K in summer to 0.25 K in winter for the ensemble mean. This response then quickly decays in the subsequent three weeks, reflecting the short time scale of the atmospheric perturbation. The initial warming impact at 850 hPa is robust, being detected in all 40 CESM ensemble members. A similarly robust impact on boundary layer inversion strength (green curves) is found in summer, fall, and winter. In summer, the inversion's response to latent heat flux convergence is similar to the 850-hPa temperature response, which indicates little-to-no warming near the surface. In summer, it is likely that an anomalous downward longwave radiation flux to the surface, associated with the 850-hPa temperature change, goes into sea ice melt rather than warming. This mechanism is further detailed in the following section. In fall and winter, however, the initial ($\tau = 1$) positive inversion strength response is weaker than the 850-hPa temperature response. Furthermore, after four weeks ($\tau = 4$), the inversion strength response switches from positive to weakly negative in some CESM ensemble members, especially in winter. This change in sign implies that a secondary warming response to latent heat flux convergence appears near the Arctic surface. The near-surface warming response begins weaker than the 850-hPa warming response, but eventually exceeds 850-hPa warming after four weeks. This fall/winter temperature response follows a similar timeline to prior observation-based studies of Arctic moist intrusions (Woods and Caballero 2016): the temperature response is initially slower at the surface than in the troposphere, but the situation eventually reverses. Such related studies have focused strictly on strong, highly localized moist intrusions, which produce surface temperature anomalies up to an order of magnitude larger than the warming tracked by our causal effect networks. The moist transport perturbations in this study are less strictly defined, as our networks track the response to any positive anomaly in Arctic-averaged latent heat flux convergence at 500 hPa. In spring, the inversion strength response to latent heat flux convergence is weak or insignificant (i.e., zero), with causal effects detected in only half of CESM ensemble members.

The total causal effect of weakened sensible heat flux convergence is shown in Fig. 5b ($-1\sigma - \nabla_{850} \cdot c_p[\overline{vT}]$) for the same time lags. In all seasons, fewer ensemble members detect a significant causal impact on Arctic temperatures, and the significant causal effects are generally smaller in magnitude and inconsistent in sign. For instance, 11 out of 40 ensemble members detect a wintertime 850-hPa warming response to weakened sensible heat flux convergence, while the remaining ensemble members detect a cooling effect or no effect at all. The causal effect signal is even weaker if sensible heat transport is instead evaluated in the midtroposphere instead of at 850 hPa ($-1\sigma - \nabla_{500} \cdot c_p[\overline{vT}]$; see Fig. S1 in the online supplemental material). Sensible heat flux convergence anomalies only cause robust temperature changes when they are evaluated on shorter (daily) time scales, where, with the exception of spring (MAM), decreases in sensible heat flux convergence partially compensate the opposite-signed impacts of a latent heat flux convergence increase (Fig. S2). Therefore, our networks suggest that Arctic sensible heat flux convergence anomalies have small impacts on lower-tropospheric temperature on submonthly time scales. Instead, temperatures are more sensitive to the latent component (Fig. 5a). This result is somewhat counterintuitive, given the relative magnitudes of climatological heat flux convergences (Figs. 1b,c). However, prior energy budget analyses have suggested that latent energy transport influences Arctic climate more strongly than dry static energy transport (Graversen and Burtu 2016; Yoshimori et al. 2017). The total causal effects shown in Figs. 5a and 5b are consistent with these findings and are robust to tests that use a more equatorward spatial averaging boundary (60°–90°N; Fig. S3). The mechanisms determining the differential warming impacts are explored in section 3b.

We expect a -1σ step decrease in sea ice extent to influence Arctic temperatures over a longer time range compared to the atmospheric perturbations in Figs. 5a and 5b. We therefore calculate the total causal effect of sea ice loss over a longer range of time lags, up to 12 weeks ($\tau_{max} = 12$). Since more time elapses between a hypothetical sea ice perturbation and the expected Arctic warming response, causal networks with $\tau_{max} = 12$ capture the influence of sea ice loss across seasons. This interseasonal influence is shown with the total causal effects in Fig. 5c. Here, most CESM ensemble members detect causal effects from sea ice loss in the summer-to-fall (JJA → SON) and fall-to-winter (SON → DJF) transitions, demonstrating a link between fall/winter Arctic temperature changes and sea ice loss in the preceding melt season. During these seasonal transitions, the Arctic warming response to sea ice loss peaks 4–6 weeks after the imposed perturbation, where ensemble-mean 850-hPa temperature changes are comparable in magnitude to those caused by enhanced latent heat flux convergence (Fig. 5a). However, the causal effect of sea ice loss at 850 hPa is dwarfed by concurrent decreases in boundary layer inversion strength, with total causal effects at $\tau = 6$ ranging from 0.5 to 1.5 K. The inversion strength response indicates a larger warming response to sea ice loss near the surface. Similar results are obtained when testing causal effects at coarser time resolution ($\tau_{max} = 12$ months; not shown), where causal effects are largely confined to lags of 1–4 months, consistent with Fig. 5c.

In summary, the perturbations imposed to our causal networks demonstrate that 850-hPa warming is caused by both sea ice loss (Fig. 5c) and enhanced latent heat flux convergence in the Arctic midtroposphere (Fig. 5a). All else being equal, 850-hPa warming increases the strength of the Arctic's boundary layer temperature inversion. However, these causal effects are outweighed by strong near-surface warming caused primarily by sea ice loss in the melt season, which weakens the temperature inversion in fall and winter. Even though anthropogenic trends are removed from our network time series, the seasonality of the total causal effects in Fig. 5 are similar to the seasonality of surface-amplified warming under RCP8.5 forcing (Fig. 1a). The inversion strength response to -1σ sea ice perturbations is approximately an order of magnitude smaller than the twenty-first-century changes simulated

in CESM1-LE (Figs. 3d and 5c), but this difference is consistent with sea ice perturbations being similarly small in comparison to projected sea ice loss (Fig. 3j). The causal effects therefore suggest that the Arctic vertical warming structure shown in Fig. 1a can be produced by the cumulative impact of seasonal sea ice retreat over many years, until the Arctic becomes ice free. Similarly, projected twenty-first-century increases in midtroposphere latent heat flux convergence are approximately a factor of 5 larger than imposed causal network perturbations (Fig. 3b), implying that the cumulative impact of many moist transport events is a significant driver of Arctic temperature trends at 850 hPa, especially in winter and spring (Figs. 3c and 5a).

Finally, it is important to note that the spatial domain of our causal networks includes both ice-covered and ice-retreat regions at the end of the twenty-first century (Fig. 2a). Accordingly, we additionally explore the extent to which the inversion strength response to sea ice loss is related to weaker inversions over sea ice or to the exposure of newly open ocean. We test the sensitivity of our causal effects to open-ocean exposure by assessing sea ice loss over ice-covered and ice-retreat regimes only (Fig. S4). The sensitivity test shows that weaker inversions do occur over sea ice, and do not require the appearance of open ocean. This result is consistent with related research that found positive Arctic lapse rate feedbacks over both ice-covered and ice-retreat regions across CMIP5 (Boeke et al. 2020).

b. The mediating role of surface energy fluxes

After quantifying the Arctic temperature response to causal network perturbations, we identify which parts of the surface energy budget mediate the temperature response to latent heat flux convergence and sea ice loss, respectively. Examining these causal pathways in greater detail reveals the physical mechanisms connecting atmospheric heat transport and sea ice loss to Arctic warming. For each perturbation introduced in section 3a, we calculate the causal effect mediated by each energy budget term. We use Eq. (7) to identify the key mediating pathways in each causal network at $\tau_{\max}$ = 4 weeks for latent heat flux perturbations (corresponding to Figs. 5a and 6), and at $\tau_{\max}$ = 12 weeks for sea ice loss perturbations (corresponding to Figs. 5c and 7). We focus on the most important mediating pathways, where $\mathrm{MCE}^{k}_{j,i}(\tau)$ is nonzero for a majority (>50%) of CESM ensemble members. Then, we visualize the causal pathways in a directed time series graph (right-hand panels of Figs. 6 and 7), which depicts the causal structure for a characteristic ensemble member. Each ensemble member may feature distinct causal pathways that are not seen in other members. Accordingly, the best visual aid is provided by a characteristic causal network that features the most common mediating effects. We limit this analysis to the fall and winter implementations of the PC-algorithm, as these seasons feature robust causal effects from both enhanced latent heat flux convergence (Fig. 5a) and sea ice loss (Fig. 5c). During these seasons, we find that causal effects of each perturbation are mediated by changes in both turbulent and longwave heat fluxes at the surface, while changes in the shortwave energy budget play no significant role.

The variables mediating the 850-hPa temperature response to enhanced latent heat flux convergence are shown in Figs. 6a and 6b and the variables mediating the inversion strength response are shown in Figs. 6c and 6d at a lag of four weeks. As noted in the previous section, the total causal effect of latent heat transport is typically positive (warming) at 850 hPa (gray-shaded row of Fig. 6a) in both fall and winter, while the inversion strength response features both weakly positive (strengthening) and negative (weakening) causal effects across the CESM ensemble (gray-shaded row of Fig. 6c). The total response in each temperature variable is explained by the mediating impact of progressive changes in the surface longwave radiative flux and sea ice extent. Initially, both T_{850} and inversion strength feature a direct, positive response to $-\nabla_{500} \cdot L[\overline{vq}]$, which is damped by the negative autocorrelation (memory) of the atmospheric perturbation in subsequent weeks (Figs. 6b,d). Therefore, the total effect in gray shading (row 3, Fig. 6a) can be regarded as the direct impact of latent heat flux convergence on T_{850}, minus the negative impacts of autocorrelation (row 2, Fig. 6a) and the mediating effect of $\mathrm{LW}_{\mathrm{net}}$ (row 4, Fig. 6a). In Figs. 6c and 6d, the initial strengthening of the inversion is also accompanied by a reduction of net longwave cooling at the surface. The decrease in longwave cooling then causes sea ice to melt, in turn weakening the inversion (Fig. 6d) through near-surface warming. Consequently, after 4 weeks, near-surface warming exceeds 850-hPa warming in a majority of CESM ensemble members, and inversion strength has decreased below its initial value (Fig. 6c).

The magnitude of the indirect causal effect on inversion strength varies by season. The distribution of mediated causal effects of sea ice loss on inversion strength features larger (more negative) values in winter than in fall (cf. green and orange distributions in Fig. 6c). In other words, the total causal effect of enhanced latent heat flux convergence produces more greatly weakened temperature inversions in winter than in fall. This result suggests that latent heat transport activates a local water vapor feedback, whereby moisture increases longwave opacity in the Arctic atmosphere, warms the surface, and melts sea ice. This water vapor greenhouse effect characterizes both the reduction in net longwave surface cooling and the resultant sea ice loss seen in Fig. 6d. A minority of ensemble members additionally detect a mediating role for longwave cloud radiative effect in the causal pathways (row 7, Figs. 6a,c; effects not shown), which may represent the transition from a "radiatively clear" to a "cloudy opaque" state in the Arctic boundary layer following a moist intrusion event [as previously highlighted in Stramler et al. (2011) and Yoshimori et al. (2017)].

Using the same visual representation, Fig. 7 highlights the surface energy fluxes that mediate the Arctic temperature response to a sea ice perturbation (-1σ) in the summer-to-fall and fall-to-winter transitions, at a lag of 12 weeks. As expected, the sea ice perturbation features large, positive autocorrelation compared to the transport perturbation in Fig. 6, and the effects are sustained through the entirety of

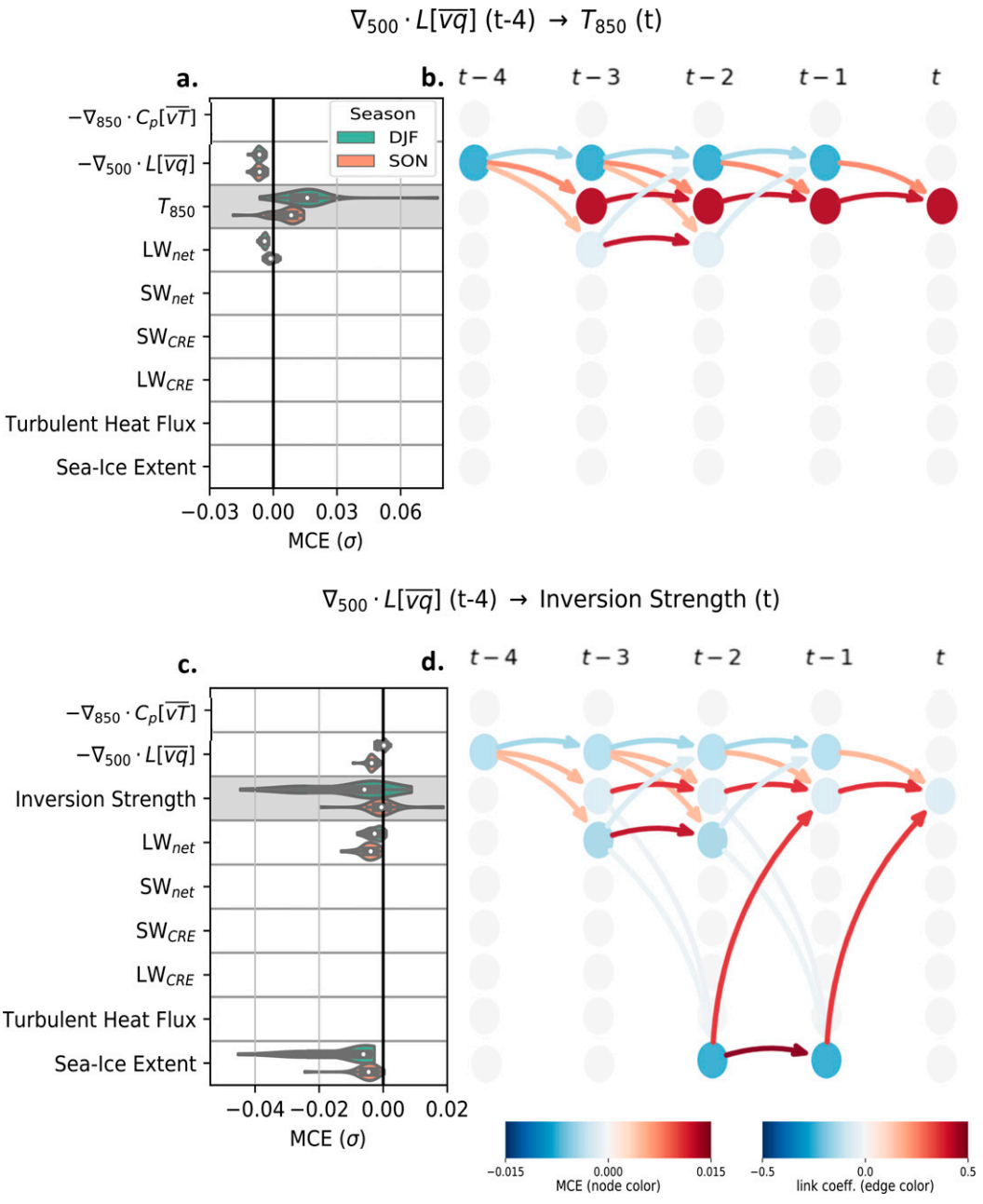

FIG. 6. Causal pathways mediating the response of 850-hPa (a),(b) Arctic temperature T_{850} and (c),(d) inversion strength to an imposed $+1\sigma$ step increase in 500-hPa Arctic latent heat flux convergence ($-\nabla_{500} \cdot L[\overline{vq}]$) at a lag of four weeks. Here (a) and (c) show the distribution of mediated causal effects in fall (SON) and winter (DJF) using violin plots, where white circles indicate a median, whiskers indicate an interquartile range, and colors indicate a probability distribution function, calculated as a nonparametric kernel density estimate. Mediated causal effects are only shown if they are nonzero in a majority (>50%) of CESM ensemble members. Note that causal effects mediated by T_{850} and inversion strength [gray-shaded rows in (a) and (c)] are equivalent to the total causal effects shown in Fig. 5a at $\tau_{max} = 4$ weeks. Panels (b) and (d) illustrate mediating causal pathways in a time series graph for CESM ensemble member 12 in fall.

the time domain in the causal networks. In the first week following a -1σ perturbation, sea ice loss causes an increase in surface longwave cloud radiative effect (LW_{CRE}) and upward turbulent heat fluxes ($t - 11$; Fig. 7b), which then mediate the eventual 850-hPa temperature response. After six weeks, these two primary mediating effects are supplemented by small changes in net longwave surface cooling and midtroposphere latent heat flux convergence (not shown). The latter

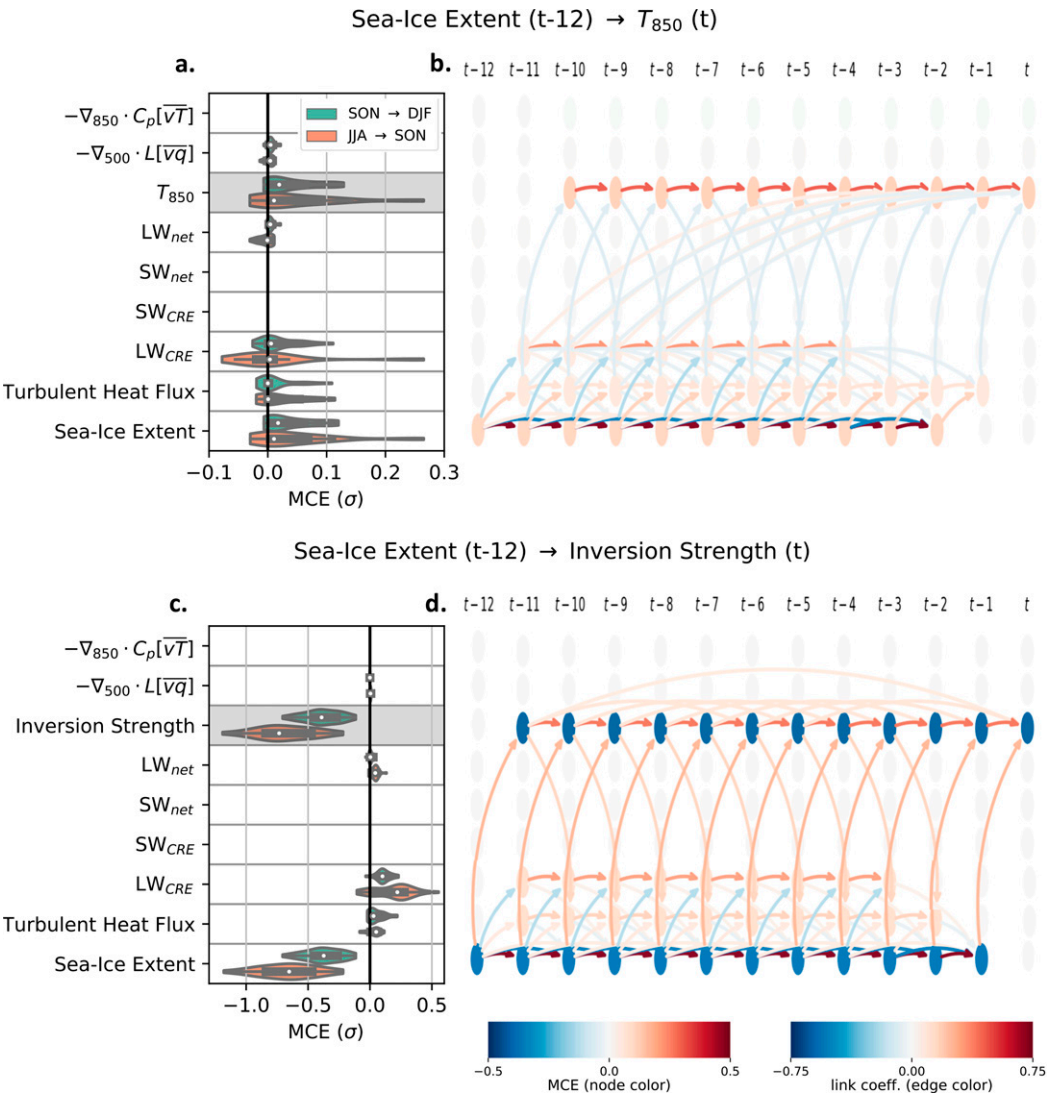

FIG. 7. Causal pathways mediating the response of 850-hPa (a),(b) Arctic temperature T_{850} and (c),(d) inversion strength to an imposed -1σ step decrease in sea ice extent at a lag of 12 weeks, shown as in Fig. 6. Panels (a) and (c) show the distribution of mediated causal effects (MCE) separately for the summer-to-fall (JJA → SON) and fall-to-winter (SON → DJF) transitions. Panels (b) and (d) show the time series graph for CESM ensemble member 3 in the fall-to-winter transition. For simplicity, visualization in (b) and (d) is limited to the primary causal pathways [MCE(12) > ±0.01].

effect is most likely associated with a poleward transport of moisture from marginal ice zones toward even higher latitudes, where the enhanced moisture supply originates from newly open ocean following a negative sea ice extent anomaly. The cloud and turbulent heat flux changes typically facilitate a warming response at 850 hPa, but the ensemble-mean response is weaker in the summer-to-fall transition, where a small subset of ensemble members feature weak cooling instead (orange distribution, Fig. 7a). Hence, the sign and magnitude of the 850-hPa temperature response is strongly linked to the seasonal mediated causal effects. The seasonal difference is particularly strong for the longwave cloud radiative effect, which tends to produce more 850-hPa cooling in the summer-to-fall transition and more 850-hPa warming in the fall-to-winter transition. However, clouds still facilitate summer-to-fall warming in some CESM ensemble members, as is the case for the example in Fig. 7b.

The weakened boundary layer inversion response to sea ice loss (Figs. 7c,d) is shaped by the same surface energy flux changes as the 850-hPa temperature response (Figs. 7a,b), but in a different manner. In both the summer-to-fall and fall-to-winter transitions, enhanced turbulent heat fluxes and longwave cloud radiative effect serve to counteract the negative total causal effect on inversion strength (Fig. 7c). In other words, the increase in upward surface energy fluxes that accompany sea ice loss reduce the weakening of the

temperature inversion. This mediating effect is accomplished by facilitating heat transfer from the near-surface to 850 hPa, consistent with the RCP8.5-forced changes in surface heat flux shown in Figs. 2b and 3i. The radiative impact of clouds also appears to reduce the surface-amplified warming response to sea ice loss, despite seasonal differences in the sign and magnitude of their impact at 850 hPa (Fig. 7a). In the following section, we attribute these seasonal differences to the vertical structure of cloud properties and associated changes in atmospheric heating rates.

c. *Characteristics of CO_2-forced reduction in boundary layer stability*

Our causal networks reveal that Arctic boundary layer inversions are weakened because of their sensitivity to sea ice perturbations in the melt season, which promote surface-amplified warming (Figs. 5c and 7c). However, the magnitude of the impact also depends on associated increases in longwave cloud radiative effect and turbulent heat fluxes, which preferentially warm 850 hPa, rather than the surface, in many CESM ensemble members (Figs. 7a,b). For the final component of our analysis, we contextualize this result by investigating the CO_2-forced response of the Arctic lower troposphere over the course of the CESM climate change simulation. This examination provides insight into the vertical extent of the atmospheric response to a step-decrease in sea ice extent, as well as its relationship to the seasonal reductions in boundary layer stability illustrated in Fig. 1a.

First, we investigate how increases in longwave cloud radiative effect could counteract the weakening inversion due to sea ice loss (Fig. 7c) while at the same time facilitating seasonally dependent temperature responses at 850 hPa (Fig. 7a). Since increases in the longwave cloud radiative effect imply enhanced downward longwave surface radiation, additional mechanisms must be considered to explain these peculiar mediating effects. Figure 8 shows projected changes in cloud altitude and total water content averaged over the Arctic Ocean. These variables are particularly useful for resolving the ambiguity because they are the primary contributors to positive longwave cloud feedbacks (Zelinka et al. 2012). In CESM-LE, the altitude of maximum Arctic Ocean cloud coverage shifts upward during fall and winter (Fig. 8a). In the same seasons, cloud water content increases throughout the lower and midtroposphere, with the largest increases in water content (10 g m^{-2}) occurring near 850 hPa (Fig. 8b). These connections are supported by reanalysis products and satellite observations in marginal sea ice zones during Arctic fall, where a deepened atmospheric boundary layer permits upward shifts in both cloud coverage and relative humidity (Schweiger et al. 2008). Cloud changes are also reflected in the changing vertical structure of atmospheric heating rates over the twenty-first century, which features increased evaporative cooling near the Arctic surface and increased condensational heating near 850 hPa (Fig. 9a, blue curves). We find that variability in LW_{CRE} is strongly correlated with 850-hPa condensational heating over sea ice regions, especially in fall ($r > 0.6$) and winter ($r > 0.8$; not shown). This correlation suggests that the near-surface warming impact of sea ice–driven LW_{CRE} increases is outweighed by concurrent increases in condensational heating at the cloud deck height (Fig. 8). Indeed, 850-hPa condensational heating experiences larger forced changes than longwave cooling rates (Fig. 9a, brown curves), which are likely associated with Arctic cloud emissivity (Curry et al. 1996; Turner et al. 2018). The RCP8.5 changes thus provide a physically plausible explanation for how an increase in LW_{CRE} may be associated with a reduced weakening of the inversion (Figs. 7c,d). We note that cloud properties and heating rates are not included in our causal networks, which prevents them from distinguishing cloud-driven longwave cooling (weakening inversion strength) from cloud-driven condensational heating (increasing inversion strength). However, the vertical profiles in Figs. 8 and 9 suggest condensational heating as the dominant mechanism.

Changes in evaporation and condensation are primarily compensated by the vertical diffusion of turbulent heat fluxes (Fig. 9a, green curves), consistent with the mediated causal effects shown in Fig. 7. Enhanced vertical diffusion near the Arctic surface corresponds to enhanced upward turbulent heat fluxes (Figs. 2b, 3i, and 7c,d), accomplishing an upward transfer of heat away from the Arctic surface. Notably, no season features changes in shortwave heating rates (Fig. 9a, orange curves). The constant shortwave atmospheric heating over the twenty-first century is consistent with the minimal cloud changes seen in summer and spring (Fig. 8), as well as our causal networks, which show that shortwave processes do not mediate the atmospheric temperature response to enhanced latent heat flux convergence (Fig. 6) or sea ice loss (Fig. 7).

The sum of these four atmospheric heating rate changes is displayed in Fig. 9b. Not surprisingly, seasons with the largest, most vertically extensive increases in net vertical heating rate are the same seasons featuring changes in boundary layer inversion strength (Fig. 1a). Winter features the largest twenty-first-century decrease in boundary layer inversion strength and the largest increase in lower tropospheric net vertical heating rate. Similar, smaller changes are seen in spring and fall. In summer, twenty-first-century Arctic warming is vertically uniform, and Fig. 9b shows negligible changes in the net heating rate. This relationship implies that when climatological temperature inversions are eroded, especially in winter, near-surface warming anomalies can be mixed upward through a larger depth of the troposphere.

4. Summary and discussion

We use causal effect networks from a fully coupled climate change simulation to quantify the Arctic's temperature sensitivity to 1σ perturbations in sea ice extent and midtropospheric atmospheric heat flux convergence. First, we show that each warming source drives distinct changes in lower-tropospheric temperatures during fall and winter. In the weeks following a step-increase in latent heat flux convergence, the Arctic lower troposphere adjusts toward more uniform warming with small net changes in boundary layer inversion strength. By contrast, sea ice loss in the melt season leads to

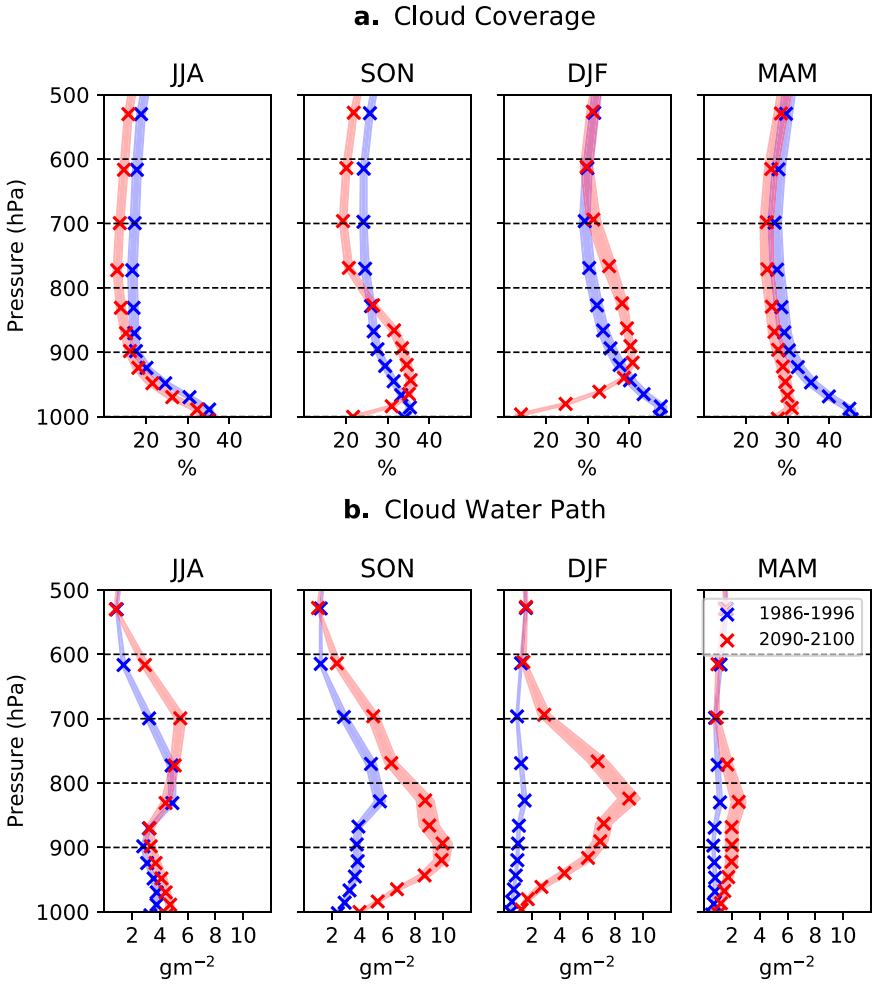

FIG. 8. The twenty-first-century, RCP8.5-forced change in Arctic atmospheric (a) cloud coverage (CLOUD) and (b) in-cloud total water path (liquid + ice; ICLDTWP) in the Community Earth System Model, Large Ensemble (CESM-LE). Vertical profiles show the Arctic-average 1986–96 (blue) and 2090–2100 (red) climatologies separately for each season, displayed as in Fig. 1. For all vertical profiles, the Arctic is defined as the spatial average within the annual mean sea ice edge (1986–96 15% concentration contour).

surface-amplified warming in fall and winter, which weakens the climatological temperature inversion. Boundary layer stability is maintained during spring and summer, which feature relatively less warming in response to sea ice loss. Taken together, these causal effects imply that, of our two proposed drivers, local sea ice loss is more important in setting the magnitude of the high-latitude lapse rate feedback. These results do not define an ultimate primary cause of Arctic-amplified warming, but rather characterize the proximate causes of T_{850} and inversion strength changes. It is ambiguous to define any variable in our causal networks as an independent control on the surface energy budget. For instance, a downward longwave radiation perturbation (associated with CO_2 forcing) could cause sea ice loss and subsequent Arctic surface warming, but downward longwave radiation is itself tightly coupled to surface temperature (Vargas Zeppetello et al. 2019). Despite this challenge, our analyses are nonetheless able to provide a robust description of how various process interactively set the Arctic vertical warming structure.

After quantifying the total causal effect of local and remote perturbations, we examine how the net Arctic warming response is mediated by changes in the surface energy budget. On multiweek time scales, we find that midtropospheric latent heat flux convergence is able to warm the Arctic surface by reducing longwave surface cooling. This indirect warming pathway, characteristic of a local water vapor feedback, is comparable to the more immediate 850-hPa temperature response, leading to only small inversion changes in fall and winter (Fig. 10), consistent with prior observation-based research on Arctic moist intrusions (Woods et al. 2013; Woods and Caballero 2016). The mediating impact of surface changes also demonstrates that moist transport can drive

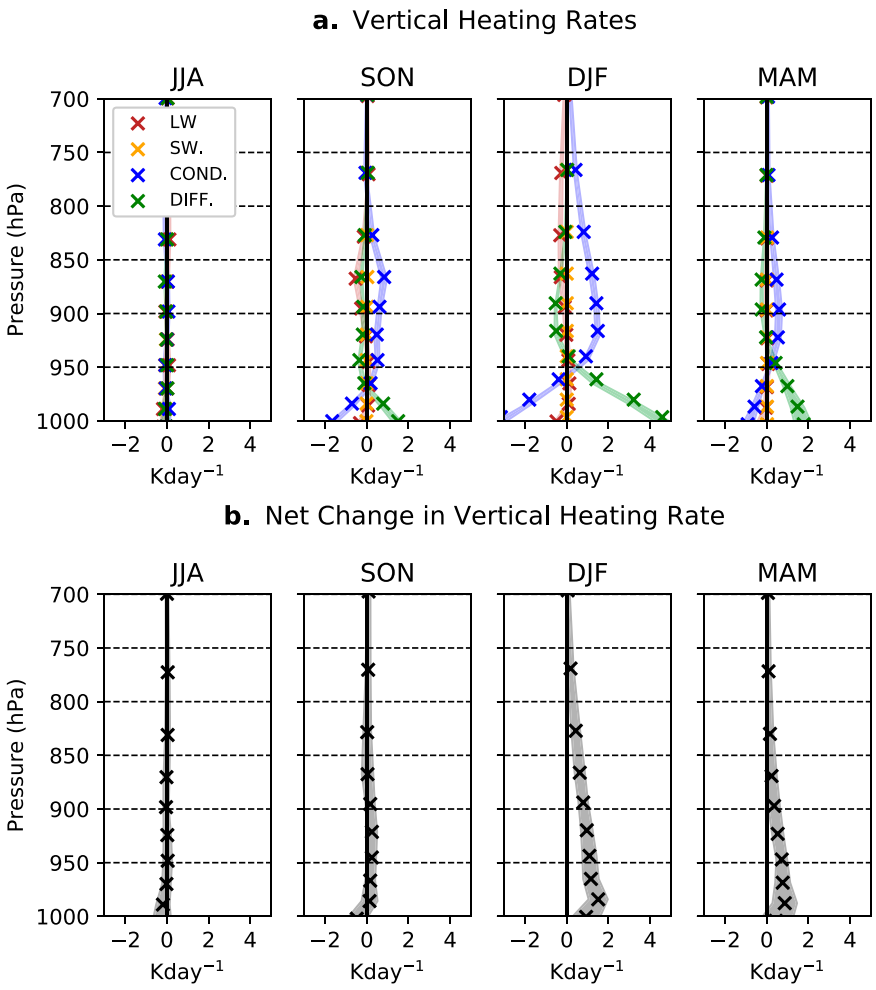

FIG. 9. The twenty-first-century, RCP8.5-forced change in vertical heating rates associated with longwave radiative cooling (LW; brown), shortwave radiative heating (SW; orange), condensational heating (COND; blue), and the vertical diffusion of turbulent heat fluxes (DIFF; green) in the Community Earth System Model, Large Ensemble (CESM-LE). Changes are calculated as the difference between the 2090–2100 and 1986–96 climatologies and are shown for (a) individual heating rates and (b) their sum (black). The CESM ensemble average and ensemble spread are separated for each season and displayed as in Fig. 8.

Arctic surface warming without lapse rate changes, even if the causal effect of sea ice perturbations dominates on longer time scales. A similar role for fast atmospheric processes has been demonstrated in recent CMIP5 experiments, where transport-driven Arctic amplification emerges before sea ice loss as a rapid response to instantaneous CO_2 quadrupling (Previdi et al. 2020). In observations and reanalyses, the fast processes are characterized by synoptic-scale atmospheric variability in Arctic moisture fluxes, which includes Rossby wave breaking and atmospheric blocking (Papritz 2020), atmospheric rivers (Baggett et al. 2016), and cyclone activity (Dufour et al. 2016).

During both fall and winter, we find that the atmospheric response to sea ice loss is facilitated by an increase in upward turbulent heat fluxes and cloud-driven condensational heating, with the vertical extent of atmospheric heating maximizing in winter; the large wintertime decreases in inversion strength are consistent with a higher cloud deck and a more extensive vertical diffusion of turbulent heat fluxes. Indeed, both observations and models have demonstrated that the cloud response to sea ice loss is regime dependent, with lower tropospheric stability controlling the altitude of the cloud deck (Barton et al. 2012). This regime dependence is also evident in the minimal cloud changes in summer, when high static stability is maintained throughout the twenty-first century. As noted in prior studies, Arctic cloud coverage and longwave optical depth can increase over newly open water if there is sufficient thermal coupling between the surface and the overlying atmosphere (Kay and Gettelman 2009; Morrison et al. 2019). As boundary layer inversions erode under anthropogenic forcing, we expect this thermal coupling will increase.

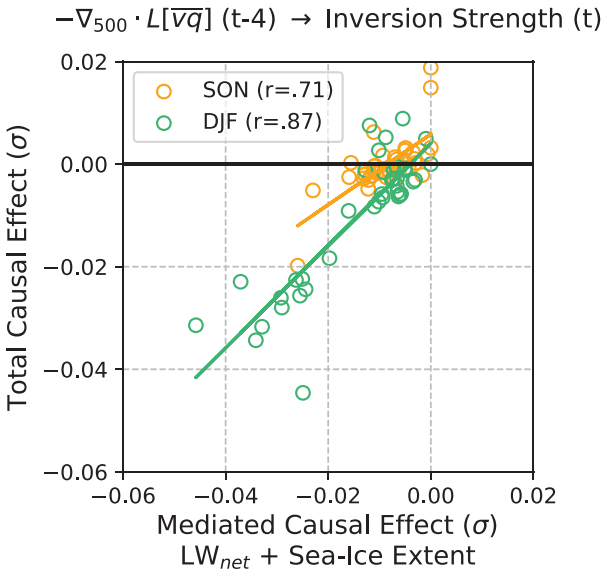

FIG. 10. The causal effect of an imposed $+1\sigma$ step increase in 500-hPa Arctic latent heat flux convergence ($-\nabla_{500} \cdot L[\overline{vq}]$) on Arctic inversion strength at a lag of four weeks (y axis) and the mediating impact of changes in surface conditions (net surface longwave radiative flux and sea ice extent; x axis). Negative causal effects indicate a weakening inversion and positive effects indicate a strengthening inversion. Values correspond to the causal effect distributions in Fig. 6c and are shown for individual CESM ensemble members (open circles) in fall (SON) and winter (DJF). The relationship between the two quantities is illustrated with Pearson correlation coefficients (r) and linear lines of best fit for each season.

This study only considers the physical representation of clouds in the CESM large ensemble, but cloud parameterization schemes remain bias-prone in the Arctic (Tan and Storelvmo 2019) and vary widely across models, causing substantial differences in climate sensitivity among them (Zelinka et al. 2020). Accordingly, future work is needed to diagnose similar cause-and-effect relationships across a range of climate models and observations. The atmospheric component of CESM1 (CAM5), for instance, is prone to lacking the cloudy state of the boundary layer in Arctic winter (Pithan et al. 2016). As a consequence, the strength of the DJF climatological temperature inversion at the start of our time series (1986–96) is likely overestimated due to strong radiative cooling (Fig. 1a). Relatedly, the DJF in-cloud total water path climatology is likely underestimated (Fig. 8b). The newly released CESM2 has addressed some of these biases, demonstrating increased total cloud liquid, downwelling surface longwave radiation, and surface temperature (McIlhattan et al. 2020).

In conclusion, our causal networks provide evidence that the vertical structure of Arctic warming is strongly tied to sea ice loss. At first, sea ice loss leads to a surface-amplified warming that is characteristic of the positive high-latitude lapse rate feedback. Once warming is large enough to erode the temperature inversion, the Arctic surface becomes more strongly coupled with the atmosphere aloft. Prior feedback studies have suggested that reduced boundary layer inversion strength will slow the rate of Arctic warming in the future; as climatological stable stratification weakens, the high-latitude lapse rate feedback may become less positive (Bintanja et al. 2011, 2012). More recent research has argued that, because the polar atmosphere is in radiative–advective equilibrium (Cronin and Jansen 2016), lapse rate changes are dependent on the type of perturbation and may be influenced by surface-based processes (Boeke et al. 2020; Feldl et al. 2020), CO_2 and water vapor increases (Henry et al. 2021), and poleward atmospheric heat transport (Feldl et al. 2017b; Henry et al. 2021; Hahn et al. 2020). While our results indicate the predominance of local warming sources (i.e., sea ice loss), the atmosphere and cryosphere exhibit different time scales of variability. Future work will seek to integrate the causal effect of step-changes in climate drivers to predict the Arctic temperature response to transient forcings. Causal network analysis offers a flexible methodology for uncovering such relationships in any set of time series, observed or simulated, without the need for targeted modeling experiments. We encourage their continued use for understanding the future evolution of climate change in the twenty-first century.

Acknowledgments. Support for Z.S.K. was provided by the National Science Foundation Graduate Research Fellowship Program under Grant NSF DGE-1842400. N.F. was supported by NSF Grant AGS-1753034.

Data availability statement. CESM Large Ensemble datasets analyzed during the current study are available on the Earth System Grid (https://www.cesm.ucar.edu/projects/community-projects/LENS/data-sets.html; Kay et al. 2015).

REFERENCES

Alexeev, V., P. L. Langen, and J. R. Bates, 2005: Polar amplification of surface warming on an aquaplanet in "ghost forcing" experiments without sea ice feedbacks. *Climate Dyn.*, **24**, 655–666, https://doi.org/10.1007/s00382-005-0018-3.

Armour, K. C., N. Siler, A. Donohoe, and G. H. Roe, 2019: Meridional atmospheric heat transport constrained by energetics and mediated by large-scale diffusion. *J. Climate*, **32**, 3655–3680, https://doi.org/10.1175/JCLI-D-18-0563.1.

Auclair, G., and L. B. Tremblay, 2018: The role of ocean heat transport in rapid sea ice declines in the Community Earth System Model large ensemble. *J. Geophys. Res. Oceans*, **123**, 8941–8957, https://doi.org/10.1029/2018JC014525.

Baggett, C., and S. Lee, 2017: An identification of the mechanisms that lead to Arctic warming during planetary-scale and synoptic-scale wave life cycles. *J. Atmos. Sci.*, **74**, 1859–1877, https://doi.org/10.1175/JAS-D-16-0156.1.

——, ——, and S. Feldstein, 2016: An investigation of the presence of atmospheric rivers over the North Pacific during planetary-scale wave life cycles and their role in Arctic warming. *J. Atmos. Sci.*, **73**, 4329–4347, https://doi.org/10.1175/JAS-D-16-0033.1.

Barton, N. P., S. A. Klein, J. S. Boyle, and Y. Y. Zhang, 2012: Arctic synoptic regimes: Comparing domain-wide Arctic cloud observations with CAM4 and CAM5 during similar

dynamics. *J. Geophys. Res.*, **117**, D15205, https://doi.org/10.1029/2012JD017589.

Bintanja, R., and E. van der Linden, 2013: The changing seasonal climate in the Arctic. *Sci. Rep.*, **3**, 1556, https://doi.org/10.1038/srep01556.

——, R. Graversen, and W. Hazeleger, 2011: Arctic winter warming amplified by the thermal inversion and consequent low infrared cooling to space. *Nat. Geosci.*, **4**, 758–761, https://doi.org/10.1038/ngeo1285.

——, E. van der Linden, and W. Hazeleger, 2012: Boundary layer stability and Arctic climate change: A feedback study using EC-Earth. *Climate Dyn.*, **39**, 2659–2673, https://doi.org/10.1007/s00382-011-1272-1.

Boeke, R. C., and P. C. Taylor, 2018: Seasonal energy exchange in sea ice retreat regions contributes to differences in projected Arctic warming. *Nat. Commun.*, **9**, 5017, https://doi.org/10.1038/s41467-018-07061-9.

——, ——, and S. A. Sejas, 2020: On the nature of the Arctic's positive lapse-rate feedback. *Geophys. Res. Lett.*, **48**, e2020GL091109, https://doi.org/10.1029/2020GL091109.

Cardinale, C. J., B. E. Rose, A. L. Lang, and A. Donohoe, 2021: Stratospheric and tropospheric flux contributions to the polar cap energy budgets. *J. Climate*, **34**, 4261–4278, https://doi.org/10.1175/JCLI-D-20-0722.1.

Cronin, T. W., and M. F. Jansen, 2016: Analytic radiative-advective equilibrium as a model for high-latitude climate. *Geophys. Res. Lett.*, **43**, 449–457, https://doi.org/10.1002/2015GL067172.

Curry, J. A., J. L. Schramm, W. B. Rossow, and D. Randall, 1996: Overview of Arctic cloud and radiation characteristics. *J. Climate*, **9**, 1731–1764, https://doi.org/10.1175/1520-0442(1996)009<1731:OOACAR>2.0.CO;2.

Dai, A., D. Luo, M. Song, and J. Liu, 2019: Arctic amplification is caused by sea-ice loss under increasing CO_2. *Nat. Commun.*, **10**, 121, https://doi.org/10.1038/s41467-018-07954-9.

Deser, C., R. Tomas, M. Alexander, and D. Lawrence, 2010: The seasonal atmospheric response to projected Arctic sea ice loss in the late twenty-first century. *J. Climate*, **23**, 333–351, https://doi.org/10.1175/2009JCLI3053.1.

Ding, Q., J. M. Wallace, D. S. Battisti, E. J. Steig, A. J. Gallant, H.-J. Kim, and L. Geng, 2014: Tropical forcing of the recent rapid Arctic warming in northeastern Canada and Greenland. *Nature*, **509**, 209–212, https://doi.org/10.1038/nature13260.

Dong, Y., C. Proistosescu, K. C. Armour, and D. S. Battisti, 2019: Attributing historical and future evolution of radiative feedbacks to regional warming patterns using a Green's function approach: The preeminence of the western Pacific. *J. Climate*, **32**, 5471–5491, https://doi.org/10.1175/JCLI-D-18-0843.1.

Dufour, A., O. Zolina, and S. K. Gulev, 2016: Atmospheric moisture transport to the Arctic: Assessment of reanalyses and analysis of transport components. *J. Climate*, **29**, 5061–5081, https://doi.org/10.1175/JCLI-D-15-0559.1.

England, M. R., I. Eisenman, N. J. Lutsko, and T. J. Wagner, 2021: The recent emergence of Arctic amplification. *Geophys. Res. Lett.*, **48**, e2021GL094086, https://doi.org/10.1029/2021GL094086.

——, S. Bordoni, and T. M. Merlis, 2017a: Coupled high-latitude climate feedbacks and their impact on atmospheric heat transport. *J. Climate*, **30**, 189–201, https://doi.org/10.1175/JCLI-D-16-0324.1.

Feldl, N., B. T. Anderson, and S. Bordoni, 2017b: Atmospheric eddies mediate lapse rate feedback and Arctic amplification. *J. Climate*, **30**, 9213–9224, https://doi.org/10.1175/JCLI-D-16-0706.1.

——, S. Po-Chedley, H. K. Singh, S. Hay, and P. J. Kushner, 2020: Sea ice and atmospheric circulation shape the high-latitude lapse rate feedback. *npj Climate Atmos. Sci.*, **3**, 41, https://doi.org/10.1038/s41612-020-00146-7.

Gong, T., S. Feldstein, and S. Lee, 2017: The role of downward infrared radiation in the recent Arctic winter warming trend. *J. Climate*, **30**, 4937–4949, https://doi.org/10.1175/JCLI-D-16-0180.1.

Graversen, R. G., and M. Wang, 2009: Polar amplification in a coupled climate model with locked albedo. *Climate Dyn.*, **33**, 629–643, https://doi.org/10.1007/s00382-009-0535-6.

——, and M. Burtu, 2016: Arctic amplification enhanced by latent energy transport of atmospheric planetary waves. *Quart. J. Roy. Meteor. Soc.*, **142**, 2046–2054, https://doi.org/10.1002/qj.2802.

——, and P. L. Langen, 2019: On the role of the atmospheric energy transport in in $2 \times CO_2$–induced polar amplification in CESM1. *J. Climate*, **32**, 3941–3956, https://doi.org/10.1175/JCLI-D-18-0546.1.

——, ——, and T. Mauritsen, 2014: Polar amplification in CCSM4: Contributions from the lapse rate and surface albedo feedbacks. *J. Climate*, **27**, 4433–4450, https://doi.org/10.1175/JCLI-D-13-00551.1.

Hahn, L., K. C. Armour, D. S. Battisti, A. Donohoe, A. Pauling, and C. Bitz, 2020: Antarctic elevation drives hemispheric asymmetry in polar lapse rate climatology and feedback. *Geophys. Res. Lett.*, **47**, e2020GL088965, https://doi.org/10.1029/2020GL088965.

Held, I. M., and B. J. Soden, 2006: Robust responses of the hydrological cycle to global warming. *J. Climate*, **19**, 5686–5699, https://doi.org/10.1175/JCLI3990.1.

Henry, M., T. M. Merlis, N. J. Lutsko, and B. E. Rose, 2021: Decomposing the drivers of polar amplification with a single-column model. *J. Climate*, **34**, 2355–2365, https://doi.org/10.1175/JCLI-D-20-0178.1.

Holland, M. M., and C. M. Bitz, 2003: Polar amplification of climate change in coupled models. *Climate Dyn.*, **21**, 221–232, https://doi.org/10.1007/s00382-003-0332-6.

Hwang, Y.-T., D. M. Frierson, and J. E. Kay, 2011: Coupling between Arctic feedbacks and changes in poleward energy transport. *Geophys. Res. Lett.*, **38**, L17704, https://doi.org/10.1029/2011GL048546.

Kay, J. E., and A. Gettelman, 2009: Cloud influence on and response to seasonal Arctic sea ice loss. *J. Geophys. Res.*, **114**, D18204, https://doi.org/10.1029/2009JD011773.

——, and Coauthors, 2015: The Community Earth System Model (CESM) Large Ensemble project: A community resource for studying climate change in the presence of internal climate variability. *Bull. Amer. Meteor. Soc.*, **96**, 1333–1349, https://doi.org/10.1175/BAMS-D-13-00255.1.

Kim, D., S. M. Kang, Y. Shin, and N. Feldl, 2018: Sensitivity of polar amplification to varying insolation conditions. *J. Climate*, **31**, 4933–4947, https://doi.org/10.1175/JCLI-D-17-0627.1.

Kostov, Y., J. Marshall, U. Hausmann, K. C. Armour, D. Ferreira, and M. M. Holland, 2017: Fast and slow responses of Southern Ocean sea surface temperature to SAM in coupled climate models. *Climate Dyn.*, **48**, 1595–1609, https://doi.org/10.1007/s00382-016-3162-z.

Kretschmer, M., D. Coumou, J. F. Donges, and J. Runge, 2016: Using causal effect networks to analyze different Arctic drivers of midlatitude winter circulation. *J. Climate*, **29**, 4069–4081, https://doi.org/10.1175/JCLI-D-15-0654.1.

Lee, S., 2012: Testing of the tropically excited Arctic warming mechanism (TEAM) with traditional El Niño and La Niña. *J. Climate*, **25**, 4015–4022, https://doi.org/10.1175/JCLI-D-12-00055.1.

——, T. Gong, S. B. Feldstein, J. A. Screen, and I. Simmonds, 2017: Revisiting the cause of the 1989–2009 Arctic surface warming using the surface energy budget: Downward infrared radiation dominates the surface fluxes. *Geophys. Res. Lett.*, **44**, 10–654, https://doi.org/10.1002/2017GL075375.

Liu, C., and E. A. Barnes, 2015: Extreme moisture transport into the Arctic linked to Rossby wave breaking. *J. Geophys. Res. Atmos.*, **120**, 3774–3788, https://doi.org/10.1002/2014JD022796.

Lu, J., and M. Cai, 2009: Seasonality of polar surface warming amplification in climate simulations. *Geophys. Res. Lett.*, **36**, L16704, https://doi.org/10.1029/2009GL040133.

Manabe, S., and R. T. Wetherald, 1975: The effects of doubling the CO_2 concentration on the climate of a general circulation model. *J. Atmos. Sci.*, **32**, 3–15, https://doi.org/10.1175/1520-0469(1975)032<0003:TEODTC>2.0.CO;2.

——, and R. J. Stouffer, 1980: Sensitivity of a global climate model to an increase of CO_2 concentration in the atmosphere. *J. Geophys. Res.*, **85**, 5529–5554, https://doi.org/10.1029/JC085iC10p05529.

McGraw, M. C., C. F. Baggett, C. Liu, and B. D. Mundhenk, 2020: Changes in Arctic moisture transport over the North Pacific associated with sea ice loss. *Climate Dyn.*, **54**, 491–506, https://doi.org/10.1007/s00382-019-05011-9.

McIlhattan, E. A., J. E. Kay, and T. S. L'Ecuyer, 2020: Arctic clouds and precipitation in the Community Earth System Model version 2. *J. Geophys. Res. Atmos.*, **125**, e2020JD032521, https://doi.org/10.1029/2020JD032521.

Merlis, T. M., and M. Henry, 2018: Simple estimates of polar amplification in moist diffusive energy balance models. *J. Climate*, **31**, 5811–5824, https://doi.org/10.1175/JCLI-D-17-0578.1.

Morrison, A., J. Kay, W. Frey, H. Chepfer, and R. Guzman, 2019: Cloud response to Arctic sea ice loss and implications for future feedback in the CESM1 climate model. *J. Geophys. Res. Atmos.*, **124**, 1003–1020, https://doi.org/10.1029/2018JD029142.

Papritz, L., 2020: Arctic lower-tropospheric warm and cold extremes: Horizontal and vertical transport, diabatic processes, and linkage to synoptic circulation features. *J. Climate*, **33**, 993–1016, https://doi.org/10.1175/JCLI-D-19-0638.1.

Park, D.-S. R., S. Lee, and S. B. Feldstein, 2015: Attribution of the recent winter sea ice decline over the Atlantic sector of the Arctic Ocean. *J. Climate*, **28**, 4027–4033, https://doi.org/10.1175/JCLI-D-15-0042.1.

Park, H.-S., S. Lee, S.-W. Son, S. B. Feldstein, and Y. Kosaka, 2015: The impact of poleward moisture and sensible heat flux on Arctic winter sea ice variability. *J. Climate*, **28**, 5030–5040, https://doi.org/10.1175/JCLI-D-15-0074.1.

Pearl, J., 2000: *Causality: Models, Reasoning, and Inference.* Cambridge University Press, 384 pp.

——, 2013: Linear models: A useful microscope for causal analysis. *J. Causal Inference*, **1**, 155–170, https://doi.org/10.1515/jci-2013-0003.

Pithan, F., and T. Mauritsen, 2014: Arctic amplification dominated by temperature feedbacks in contemporary climate models. *Nat. Geosci.*, **7**, 181–184, https://doi.org/10.1038/ngeo2071.

——, and Coauthors, 2016: Select strengths and biases of models in representing the Arctic winter boundary layer over sea ice: The Larcform 1 single column model intercomparison. *J. Adv. Model. Earth Syst.*, **8**, 1345–1357, https://doi.org/10.1002/2016MS000630.

Previdi, M., T. P. Janoski, G. Chiodo, K. L. Smith, and L. M. Polvani, 2020: Arctic amplification: A rapid response to radiative forcing. *Geophys. Res. Lett.*, **47**, e2020GL089933, https://doi.org/10.1029/2020GL089933.

Runge, J., and Coauthors, 2015: Identifying causal gateways and mediators in complex spatio-temporal systems. *Nat. Commun.*, **6**, 8502, https://doi.org/10.1038/ncomms9502.

——, and Coauthors, 2019: Inferring causation from time series in Earth system sciences. *Nat. Commun.*, **10**, 2553, https://doi.org/10.1038/s41467-019-10105-3.

Schweiger, A. J., R. W. Lindsay, S. Vavrus, and J. A. Francis, 2008: Relationships between Arctic sea ice and clouds during autumn. *J. Climate*, **21**, 4799–4810, https://doi.org/10.1175/2008JCLI2156.1.

Screen, J. A., and Coauthors, 2018: Consistency and discrepancy in the atmospheric response to Arctic sea-ice loss across climate models. *Nat. Geosci.*, **11**, 155–163, https://doi.org/10.1038/s41561-018-0059-y.

Serreze, M. C., A. P. Barrett, A. G. Slater, M. Steele, J. Zhang, and K. E. Trenberth, 2007a: The large-scale energy budget of the Arctic. *J. Geophys. Res.*, **112**, D11122, https://doi.org/10.1029/2006JD008230.

——, M. M. Holland, and J. Stroeve, 2007b: Perspectives on the Arctic's shrinking sea-ice cover. *Science*, **315**, 1533–1536, https://doi.org/10.1126/science.1139426.

——, A. Barrett, J. Stroeve, D. Kindig, and M. Holland, 2009: The emergence of surface-based Arctic amplification. *Cryosphere*, **3**, 11–19, https://doi.org/10.5194/tc-3-11-2009.

Singh, H. K., C. M. Bitz, A. Donohoe, and P. J. Rasch, 2017: A source-receptor perspective on the polar hydrologic cycle: Sources, seasonality, and Arctic–Antarctic parity in the hydrologic cycle response to CO_2 doubling. *J. Climate*, **30**, 9999–10017, https://doi.org/10.1175/JCLI-D-16-0917.1.

Smith, D. M., and Coauthors, 2019: The Polar Amplification Model Intercomparison Project (PAMIP) contribution to CMIP6: Investigating the causes and consequences of polar amplification. *Geosci. Model Dev.*, **12**, 1139–1164, https://doi.org/10.5194/gmd-12-1139-2019.

Spirtes, P., C. N. Glymour, R. Scheines, and D. Heckerman, 2000: *Causation, Prediction, and Search.* MIT Press, 543 pp.

Stramler, K., A. D. Del Genio, and W. B. Rossow, 2011: Synoptically driven Arctic winter states. *J. Climate*, **24**, 1747–1762, https://doi.org/10.1175/2010JCLI3817.1.

Stuecker, M. F., and Coauthors, 2018: Polar amplification dominated by local forcing and feed backs. *Nat. Climate Change*, **8**, 1076–1081, https://doi.org/10.1038/s41558-018-0339-y.

Tan, I., and T. Storelvmo, 2019: Evidence of strong contributions from mixed-phase clouds to Arctic climate change. *Geophys. Res. Lett.*, **46**, 2894–2902, https://doi.org/10.1029/2018GL081871.

Tomas, R. A., C. Deser, and L. Sun, 2016: The role of ocean heat transport in the global climate response to projected Arctic sea ice loss. *J. Climate*, **29**, 6841–6859, https://doi.org/10.1175/JCLI-D-15-0651.1.

Turner, D., M. Shupe, and A. Zwink, 2018: Characteristic atmospheric radiative heating rate profiles in Arctic clouds as observed at Barrow, Alaska. *J. Appl. Meteor. Climatol.*, **57**, 953–968, https://doi.org/10.1175/JAMC-D-17-0252.1.

Vargas Zeppetello, L., A. Donohoe, and D. Battisti, 2019: Does surface temperature respond to or determine downwelling longwave radiation? *Geophys. Res. Lett.*, **46**, 2781–2789, https://doi.org/10.1029/2019GL082220.

Winton, M., 2006: Amplified Arctic climate change: What does surface albedo feedback have to do with it? *Geophys. Res. Lett.*, **33**, L03701, https://doi.org/10.1029/2005GL025244.

Woods, C., and R. Caballero, 2016: The role of moist intrusions in winter Arctic warming and sea ice decline. *J. Climate*, **29**, 4473–4485, https://doi.org/10.1175/JCLI-D-15-0773.1.

——, ——, and G. Svensson, 2013: Large-scale circulation associated with moisture intrusions into the Arctic during winter. *Geophys. Res. Lett.*, **40**, 4717–4721, https://doi.org/10.1002/grl.50912.

Yoshimori, M., A. Abe-Ouchi, and A. Laîné, 2017: The role of atmospheric heat transport and regional feedbacks in the Arctic warming at equilibrium. *Climate Dyn.*, **49**, 3457–3472, https://doi.org/10.1007/s00382-017-3523-2.

Zelinka, M. D., S. A. Klein, and D. L. Hartmann, 2012: Computing and partitioning cloud feedbacks using cloud property histograms. Part II: Attribution to changes in cloud amount, altitude, and optical depth. *J. Climate*, **25**, 3736–3754, https://doi.org/10.1175/JCLI-D-11-00249.1.

——, T. A. Myers, D. T. McCoy, S. Po-Chedley, P. M. Caldwell, P. Ceppi, S. A. Klein, and K. E. Taylor, 2020: Causes of higher climate sensitivity in CMIP6 models. *Geophys. Res. Lett.*, **47**, e2019GL085782, https://doi.org/10.1029/2019GL085782.